COLLECTIVE INFORMATION PROCESSING IN SYNTHETIC MORPHOGENIC LIPOSOMES AND HYBRID CELL-COMPUTER WOUND HEALING WITH OPTOGENETICALLY EMULATED SIGNALING

Bruno Scocozza

Zur Erlangung des akademischen Grades eines
Doktors der Naturwissenschaften
(Dr. rer. nat.)

der Fakultät Chemie und Chemische Biologie
der Technischen Universität Dortmund

December 2020

Vorgelegt im December 2020

von Bruno Scocozza

Gutachter:

Prof. Dr. Philippe I. H. Bastiaens

Prof. Dr. Roland Winter

The work presented in this dissertation was performed in the laboratory of Prof. Dr. Philippe I.H. Bastiaens at the Max Planck Institute of Molecular Physiology, Dortmund, Germany.

The work described in this thesis has partly been included in the following publications:

Konstantin Gavriljuk, Bruno Scocozza, Farid Ghasemalizadeh, Akhilesh P. Nandan, Manuel Campos Medina, Hans Seidel, Malte Schmick, Aneta Koseska, Philippe I. H. Bastiaens, *A synthetic morphogenic membrane system that responds with self-organized shape changes to local light cues* bioRxiv, 2019

Eidesstattliche Versicherung (Affidavit)

Name, Vorname
(Surname, first name)

Matrikel-Nr.
(Enrolment number)

Belehrung:

Wer vorsätzlich gegen eine die Täuschung über Prüfungsleistungen betreffende Regelung einer Hochschulprüfungsordnung verstößt, handelt ordnungswidrig. Die Ordnungswidrigkeit kann mit einer Geldbuße von bis zu 50.000,00 € geahndet werden. Zuständige Verwaltungsbehörde für die Verfolgung und Ahndung von Ordnungswidrigkeiten ist der Kanzler/die Kanzlerin der Technischen Universität Dortmund. Im Falle eines mehrfachen oder sonstigen schwerwiegenden Täuschungsversuches kann der Prüfling zudem exmatrikuliert werden, § 63 Abs. 5 Hochschulgesetz NRW.

Die Abgabe einer falschen Versicherung an Eides statt ist strafbar.

Wer vorsätzlich eine falsche Versicherung an Eides statt abgibt, kann mit einer Freiheitsstrafe bis zu drei Jahren oder mit Geldstrafe bestraft werden, § 156 StGB. Die fahrlässige Abgabe einer falschen Versicherung an Eides statt kann mit einer Freiheitsstrafe bis zu einem Jahr oder Geldstrafe bestraft werden, § 161 StGB.

Die oben stehende Belehrung habe ich zur Kenntnis genommen:

Official notification:

Any person who intentionally breaches any regulation of university examination regulations relating to deception in examination performance is acting improperly. This offence can be punished with a fine of up to EUR 50,000.00. The competent administrative authority for the pursuit and prosecution of offences of this type is the chancellor of the TU Dortmund University. In the case of multiple or other serious attempts at deception, the candidate can also be unenrolled, Section 63, paragraph 5 of the Universities Act of North Rhine-Westphalia.

The submission of a false affidavit is punishable.

Any person who intentionally submits a false affidavit can be punished with a prison sentence of up to three years or a fine, Section 156 of the Criminal Code. The negligent submission of a false affidavit can be punished with a prison sentence of up to one year or a fine, Section 161 of the Criminal Code.

I have taken note of the above official notification.

Ort, Datum
(Place, date)

Unterschrift
(Signature)

Titel der Dissertation:
(Title of the thesis):

Ich versichere hiermit an Eides statt, dass ich die vorliegende Dissertation mit dem Titel selbstständig und ohne unzulässige fremde Hilfe angefertigt habe. Ich habe keine anderen als die angegebenen Quellen und Hilfsmittel benutzt sowie wörtliche und sinngemäße Zitate kenntlich gemacht.
Die Arbeit hat in gegenwärtiger oder in einer anderen Fassung weder der TU Dortmund noch einer anderen Hochschule im Zusammenhang mit einer staatlichen oder akademischen Prüfung vorgelegen.

I hereby swear that I have completed the present dissertation independently and without inadmissible external support. I have not used any sources or tools other than those indicated and have identified literal and analogous quotations.

The thesis in its current version or another version has not been presented to the TU Dortmund University or another university in connection with a state or academic examination.*

*Please be aware that solely the German version of the affidavit ("Eidesstattliche Versicherung") for the PhD thesis is the official and legally binding version.

Ort, Datum
(Place, date)

Unterschrift
(Signature)

“VERKÖRPERUNG DES *SINNS*

Der SINN, den man ersinnen kann,
ist nicht der ewige SINN.
Der Name, den man nennen kann,
ist nicht der ewige Name.
Jenseits des Nennbaren liegt der Anfang der Welt.
Diesseits des Nennbaren liegt die Geburt der Geschöpfe.
Darum führt das Streben nach dem Ewig-Jenseitigen
zum Schauen der Kräfte,
das Streben nach dem Ewig-Diesseitigen
zum Schauen der Räumlichkeit.
Beides hat Einen Ursprung und nur verschiedenen Namen.
Diese Einheit ist das Große Geheimnis.
Und des Geheimnisses noch tieferes Geheimnis:
Das ist die Pforte der Offenbarwerdung aller Kräfte.”

“The DAO that can be expressed
is not the eternal DAO.
The name that can be named
is not the eternal name.

“Non-existence” I call the beginning of Heaven and Earth.
“Existence” I call the mother of individual beings.

Therefore does the direction towards non-existence
lead to the sight of the miraculous essence,
the direction towards existence
to the sight of spatial limitations.

Both are one in origin
and different only in name.
In its unity it is called the secret.
The secret’s still deeper secret:
is the gateway through which all miracles emerge.”

Tao Te King, Lao Tse,

Translated into German by Richard Wilhelm (Jena, 1911, Eugen Diederichs),
then into English by H.G. Ostwald (London, 1985, Arkana)

ABSTRACT

Throughout the different scales at which living organisms operate, it is the collective behaviour between the entities that compose them that determines their identity and function. Biomolecules, cells and whole organisms interact to process information and generate organization at the subcellular, tissue and ecosystem scales.

In the first part of this thesis, we investigated fundamental principles of cellular morphogenesis in response to external cues in a Synthetic Morphogenic Membrane System (SynMMS). SynMMS was composed of an encapsulated dynamic microtubule (MT) aster, together with a light-inducible signal transduction system in cell-sized liposomes. We show that light-activated signaling induces MT growth through activation of an activity gradient of the MT-regulator stathmin. SynMMSs are thus capable of responding to local external light cues with directed morphological changes, as if originating from an extracellular morphogen. Morphometric analysis methods enabled us to uncover feedbacks within and among the signaling and cytoskeletal subsystems, which are mediated by the deformable membrane. We found that bi-directional interactions between the signaling and MT-aster system underlie the creation of self-organized morphologies as well as their reorganization in the direction of external light cues.

In the second part, we develop a novel method to investigate how at a higher scale, the coupling of such intracellular processing networks leads to functional collective behaviour. We develop a hybrid cell-computer experimental interface to create hybrid wound healing assays, in which living cells are recruited to a virtual wound while undergoing virtual paracrine signaling. The migration state of cells is measured in real time from which *in silico* cell-to-cell communication is computed and translated into optogenetic actuation that induces cell migration, emulating extracellular signaling cues. The hybrid assay phenocopies features of *in vivo* neutrophil swarming towards an injury, demonstrating that a paracrine signaling relay allows expanding the recruitment region. Thus, this method allows to create hybrid *in vitro-in silico* dynamics where the influence of intercellular communication parameters can be quantitatively investigated.

Altogether, investigation of collective behaviour in synthetic proto-cells uncovered how MT-signaling interactions determine cellular morphogenesis, while hybrid cell-computer interfaces establish a new method for quantitative interrogation of cellular communication during tissue morphogenesis.

ZUSAMMENFASSUNG

In allen Dimensionen in denen Leben agiert, ob zellulär, in Geweben oder als ganzes Ökosystem, kommt es auf das Zusammespiel der einzelnen Instanzen (Proteine, Zellen oder Organismen) an. Die Informationsverarbeitung der kleinsten Einheiten bestimmt die Identität und Funktion des Ganzen.

Im ersten Teil dieser Arbeit wurden fundamentale Prinzipien der Zellmorphogenese unter Einfluss von Umgebungsreizen in einem synthetischen morphogenetischen Membransystem (SynMMS) untersucht. Bei diesem System handelt es sich um ein dynamisches Mikrotubuli-(MT) Aster, das zusammen mit einem lichtinduzierbaren Signaltransduktionssystem in ein zellgroßes Liposom eingeschlossen wurde. Es konnte gezeigt werden, dass lichtinduzierte Signaltransduktion ein lokales MT Wachstum hervorruft welches durch einen Aktivitätsgradienten des MT-regulators Stathmin gesteuert wurde. Folglich ist das SynMMS fähig, auf externe Lichtreize zu reagieren. Hierdurch werden gerichteten morphologischen Veränderungen hervorgerufen, welche analog zu Veränderungen sind, die durch extrazellulären Morphogene in Zellen induziert werden können. Morphometrische Analysemethoden haben es ermöglicht Rückkopplungen innerhalb der Signaltransduktion oder dem Zytoskelett-Subsystem sowie zwischen diesen zu entschlüsseln. Hierdurch wurde deutlich, dass die Verformbarkeit der Membran die rekursiven Interaktionen zwischen der Signalübertragung und dem MT-Aster System ermöglicht. Diese Interaktionen widerrum ermöglichen es, dass selbstorganisierte morphologischen Strukturen in Richtung von Lichtimpulsen umorganisieren.

Im zweiten Teil der Arbeit wurde untersucht wie die Kommunikation von zellulären Netzwerken zu kollektiven Verhalten führt. Um dies zu ermöglichen, wurde eine neue Methode entwickelt: eine hybride Zell-Computer-Schnittstelle in der eine Verbinding zwischen lebenden Zellen und virtueller Kommunikation geschaffen wurde. Dies Methode basiert auf einem Wundheilungsexperiment, worin lebende Zellen zu einer virtuellen Wunde hin rekrutiert wodurch virtuelle parakrine-basierte Kommunikation ausgelöst wurde. Die Zellmigration wurde in Echtzeit gemessen wodurch *in silico* die Zell-Zell Kommunikation berechnet wurde und anschließend in optogentische Stimulation übersetzt wurde. Die optogenetische Stimulation imitiert die extrazellulären Signalreize wodurch Zellmigration ausgelöst wurde. Das Hybrid-System rekapituliert das Verhalten neutrophiler Granulozyten *in vivo* und demonstriert, dass parakrine Signalübertragung den Rekrutierungsbereich für Zellen graduell

erweitert. Somit erzeugte diese Methode eine hybride *in-vitro-in-silico*-Dynamik, mit welcher der Einfluss interzellulärer Kommunikationsparameter quantitativ untersucht werden konnte.

Insgesamt zeigten die Untersuchung des kollektiven Verhaltens in synthetischen Systemen, wie MT-Signalwechselwirkungen die zelluläre Morphogenese bestimmen, während die Methode der hybriden Zell-Computer-Schnittstelle zur quantitativen Abfrage der zellulären Kommunikation während der Gewebsmorphogenese zur Wundheilung diente.

CONTENTS

LIST OF FIGURES

LIST OF ABBREVIATIONS AND ACRONYMS

PBRW	Persistent Biased Random Walk
OU	Ornstein-Uhlenbeck
MEF	Mouse Embryonic Fibroblast
RCS	Relative Centrosome Surface
SynMMS	Synthetic Morphogenic Membrane System
SIC	Self-induced capture
MT	Microtubule
GUV	Giant unilamellar vesicle
iLID	improved Light-Induced Dimer
GTP	Guanosine-5'-triphosphate
fMLP	N-formyl-L-methionyl-L-leucyl-phenylalanine
LTB4	Leukotriene B4
2P-IVM	Two-photon intravital microscopy
PA-Rac1	Photoactivatable Rac1
LOV	Light Oxygen Voltage

1 INTRODUCTION

1.1 Collective behavior in living systems

In the past century, biological studies have been very successful in finding and characterizing molecular components as well as molecular interactions involved in many biological functions. However, the understanding of the individual entities themselves does not suffice to understand the complex behavior of living matter. Throughout the different scales at which living organisms operate, it is the collective behavior of the entities that compose them which underlies the information processing systems that determine their identity and function. Biomolecules, cells and whole organisms couple their own information processing capabilities to generate organization at the higher scales, namely, subcellular, tissue, single organism and entire ecosystems. Therefore, the study of collective behavior focuses on understanding how the activities of individual, but intercommunicating entities, leads to higher scale functions at the collective level.

Collective behavior occurs at all layers of biological organization, from molecular systems to entire ecosystems. At the higher scales, millimeter-size termites build meter-sized mounds as microhabitats to protect themselves from environmental changes[1,2], bacteria form rafts for coordinated swarming[3], locust plague-insects coordinate mass migration through cannibalistic interactions[4], migrant birds exploit social information during flights[5,6], etc. At the cellular and subcellular scales, complex molecular systems equip living cells with multiple sensory and actuation systems, which can be studied as complex dynamical systems. These systems contain enough richness to allow for cells to simultaneously represent the external information from the environment, as well as to process it and respond accordingly. At the tissue scale, intercellular communication entangles the individual processing networks, which leads to coordination in their behavior to attain functions such as tissue morphogenesis, differentiation, and tissue repair, among others. This is a result of intercellular communication, by which cells can expand their intracellular dynamical solutions[7]. At all these levels, communication is the fundamental feature that enables information flow among the entities, to collectively perceive their environment and conduct functions which the individual entities cannot attain by themselves.

In the following sections we will introduce the biological systems involved in morphogenesis whose collective behaviour was investigated in this thesis. We will also introduce the problem of observability and perturbation of such systems.

1.2 Microtubule cytoskeleton

Eukaryotic cells have evolved a myriad of mechanisms for perceiving, storing and processing extracellular information in order to adapt or maintain their identity in a changing environment. Cell morphology plays a significant role in biological function through dynamic cytoskeletal systems which are mainly composed of actin filaments, intermediate filaments and microtubules (MTs). These cytoskeletal systems are responsible for changes in cell shape and motility, exhibiting different characteristic length and time scales[8]. Actin filaments are formed of actin monomers that polymerize to form filaments, which can cross-link to form meshed networks. Microtubules, instead, are composed of tubulin dimers which polymerize in the presence of Guanosine-5'-triphosphate (GTP) and are both thicker and stiffer than actin. In many cell types, MTs are organized through MT organizing centers (MTOC), which leads to MT-asters with MTs radiating from the center to the peripheral regions. Therefore, MTs are globally organized and coordinated, acting at the scale of the cell, playing a fundamental role in polarity as well as the establishment and stabilization of cell shape during differentiation[9–13].

MTs can rapidly alternate between phases of slow grow and fast shrinkage, a behavior known as dynamic instability (Figure 1.1) [14,15]. This highly dynamic process exhibits two main phases: the process of growing after shrinking is known as rescue, while the transition from growth to shrinkage is known as catastrophe. MT dynamics can be largely described by four parameters: (i) shrinkage speed, (ii) growth speed, (iii) catastrophe frequency, and (iv) rescue frequency. Importantly, both the growth velocity and the catastrophe frequency have been shown to depend on the concentration of tubulin heterodimers available for polymerization[16] (free tubulin). The discovery of dynamic instability presented a mechanism by which cells can rearrange their MT-cytoskeleton, for example, during the cell cycle. Regulation of MT dynamics is thus crucial for accomplishing functions such as the segregation of chromosomes, polarization, directional migration and differentiation, among others. To attain these functions, cells must employ mechanisms to control and direct the organization of the MT cytoskeleton in response to external cues.

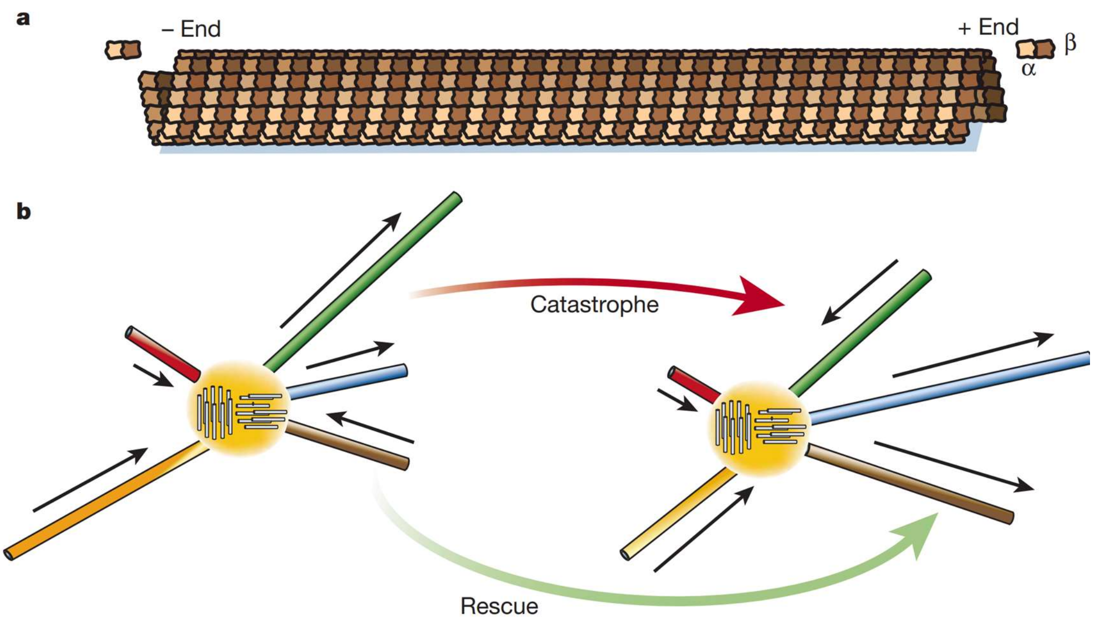

Figure 1.1: Microtubule dynamic instability

(a) A microtubule lattice is shown where dark-light brown heterodimers represent α/β tubulin dimers. (b) Representation of microtubules attached to a MT-organizing center undergoing phases of growth and shrinkage. Each color represents a single MT at different times. Red and yellow MTs undergo constant shrinkage, blue MT is shown to be in a phase of growth. The MT in green undergoes a "catastrophe" event, in which growth transitions to shrinkage, while the brown MT undergoes rescue, in which shrinkage is followed by growth. (Reprinted by permission from Springer Nature: [17], Copyright © 2003).

1.3 Morphogen induced reorganization of the MT cytoskeleton

In cells, re-organization of the cytoskeleton is directed by extracellular morphogens such as growth factors and chemoattractants, which act by inducing localized signaling reactions that generate cytoplasmic activity of MT-associated proteins (MAPs). MAPs interact with MTs regulating their dynamics by, for example, stabilizing, destabilizing or bundling MTs[18]. The transduction of external signals into cytoskeletal reorganization via MAPs takes place through complex signaling networks such as the canonical Rac1-PAK1-stathmin MT-regulator network (Figure 1.2) [19–22]. Morphogen-induced activation of RhoGTPases such as Rac1 leads to plasma membrane recruitment and activation of kinase effectors such as Pak1. Pak1 then phosphorylates the MT-regulator stathmin, diminishing its tubulin sequestration capability, thereby increasing the availability of free tubulin for MT growth.

In the absence of stimulus, the kinase remains in the cytosol, where the high activity of phosphatases maintain low steady state phosphorylation levels of stathmin, thereby constraining MT growth. Upon localized external signals, the reduction in dimensionality[23,24] of effectors, from cytosolic (3D) to membrane localized (2D), causes a substantial increase in their concentration, accompanied by a reduction in their mobility. This increases the effective concentration and hence the kinase activity to its cytosolic substrate stathmin on the stimulated region. Together with diffusion of cytosolic MAPs such as stathmin, this leads to gradients of activity within the cell[24], emanating from morphogen exposed areas. This local spatial rebalancing of reaction cycles enables directing cytoskeletal re-organization in the direction of the morphogen cue by local modulation of MAP activity (Figure 1.2c).

1.4 Relation of cell morphology to signaling

At the same time, prior work has shown that signaling activity can be affected by geometric features of the plasma membrane, even in the presence of uniform signals[25]. Different plasma membrane curvatures have different local surface (membrane) to volume (cytosol) ratios. For reactions occurring between cytosolic and membrane localized molecules, curvature and diffusion will therefore determine diffusional access of cytosolic reactants to the membrane proximal region. When cytosolic molecules react with membrane localized molecules to form a product at the membrane, the concentration of the product is transiently enhanced in low curvature regions, due to faster replenishment of substrate. Similarly, this effects can occur for reactions between extracellular and membrane localized molecules, where the topology is inverted. Based on this findings, other authors postulated the existence of an interdependence between signaling and membrane shape, in which a recursion between cytoskeleton induced deformation and signaling activity at the membrane underlies morphogenesis[26]. In this sense, the rapid remodeling of the plasma membrane by the cytoskeleton may constantly produce transient enhancements in the sensing of extracellular morphogens as well as their transduction into different local signaling activities. This studies thus suggest that the cytoskeleton induced cell shape is tightly linked to the information processing capabilities of cells.

In the first part of this thesis, we use synthetic morphogenic proto-cells to investigate mechanisms of interaction between signaling and MT-aster induced shape and how this interaction is related to information processing of external cues.

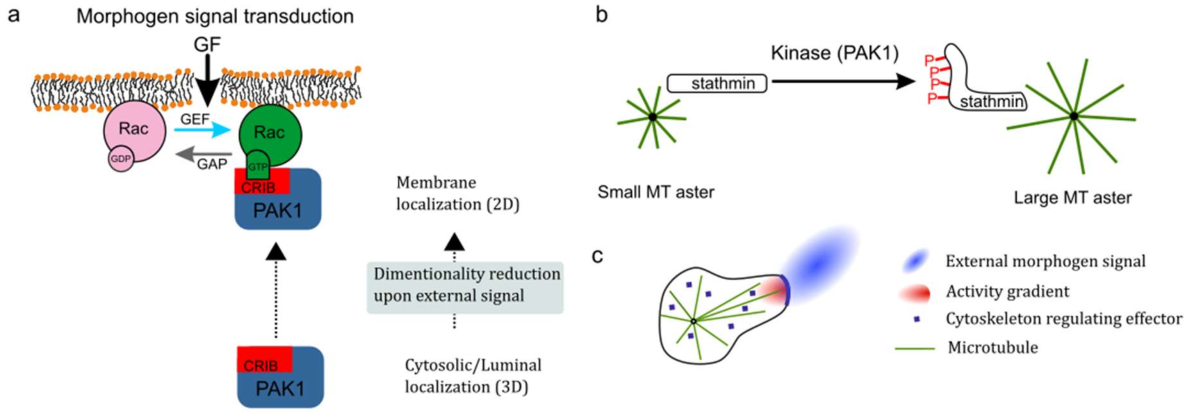

Figure 1.2: Schemes of Rac1-PAK1-stathmin MT-regulator network

(a) Activation of morphogen transduction network by growth factor (GF) induced translocation of PAK1 to activated Rac1-GTP at the plasma membrane and (b) subsequent phosphorylation of stathmin by the activated PAK1. (c) Local morphogen signals induce local activity gradients of the cytoskeleton regulator molecules biasing the response in the direction of the signal. GEF: guanine nucleotide exchange factor, GAP: GTPase activating protein. Diagrams adapted from [16].

1.5 Wound healing

The cellular mechanisms described above allow individual cells to represent the information of the environment and equip them with potential response mechanisms, such as directed morphogenesis. For ensembles of living cells to accomplish higher scale functions, intercellular communication entangles the individual cellular processing networks, leading to coordination in their behaviour.

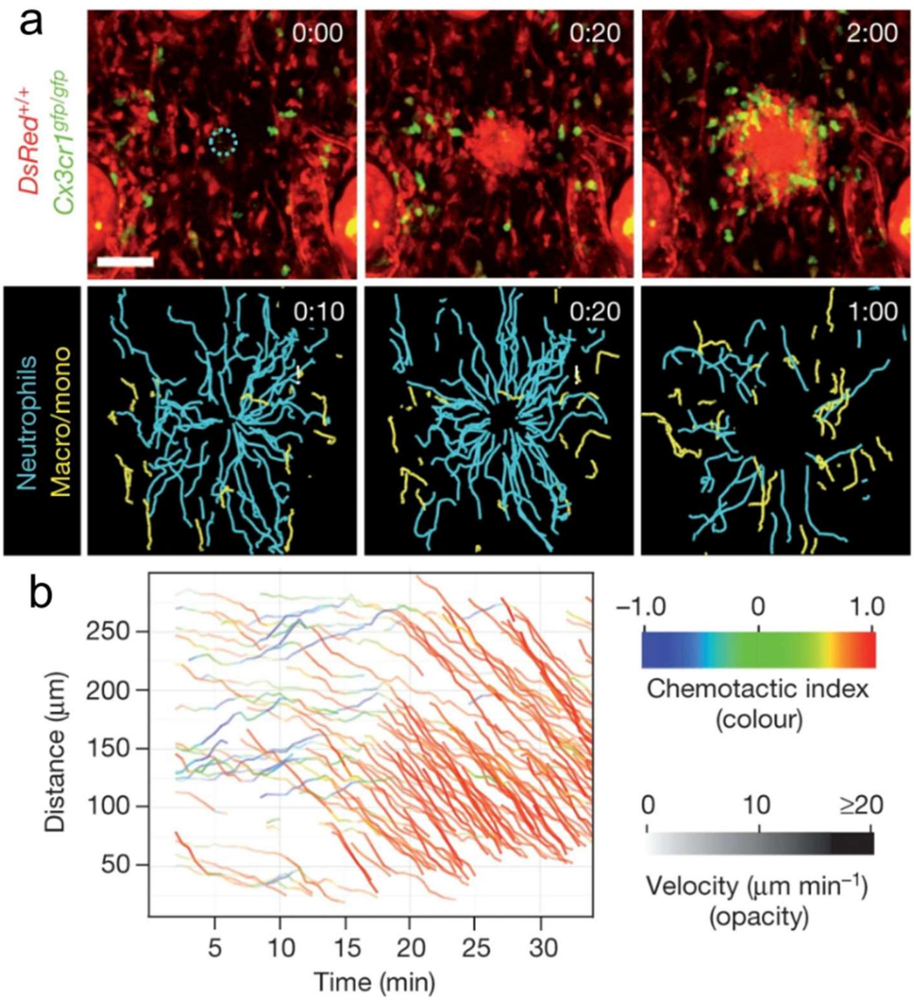

Figure 1.3: Neutrophil swarming dynamics towards an injury site.
Two-photon intravital microscopy showing cell recruitment towards a focus damage site (blue dotted circle). (a) Top: Time-lapse of endogenous innate immune cell response in DsRed$^{+/+}$ Cx3cr1$^{gfp/gfp}$ Tyrc$^{-2J/c-2J}$ mice (green: macrophages/monocytes, red: neutrophils and stroma). Bottom: Tracks for cells over the 10 minutes at the shown timepoints (h:min). (b) Distance to the center of the wound vs. time, color-coded by chemotactic index and velocity for intradermal injected bone marrow neutrophils. (Reprinted from [27] with permission, Copyright © 2013, Springer Nature)

This is the case during the fundamental process of wound healing, where multiple cell types coordinate their behavior to restore healthy tissue. In particular, neutrophil recruitment to sites of tissue damage is a hallmark of immune system response and has been studied employing different experimental models. Among them, mouse models of inducible sterile skin injury have been developed, where a short two-photon laser pulse causes tissue damage, leading to directed cell migration towards the wound site[27] (Figure 1.3). This process exhibits several stages[28]: firstly, the injury is created, where cell death leads to the release of intracellular content. This molecules can then act as signaling molecules for the cells surrounding the injury, some of which will directly react to the injury. The activity of this primary responding cells can then trigger the response of other cells, be it from the same or from different cell types, whose actions aid in closing the wound and restoring normal tissue.

In the case of neutrophils, a first phase of neutrophil recruitment from sites close to the wound is observed, followed by delayed recruitment from distant sites[27]. Previous studies have shown that in response to the primary chemoattractant fMLP (N-formyl-L-methionyl-L-leucyl-phenylalanine), neutrophils produce a secondary chemoattractant signal by secreting the leukotriene B4 (LTB4) [27,29]. It was also shown that LTB4 plays a significant role in sensitizing neutrophils to the primary chemoattractant by facilitating polarization in the direction of the cue[29]. This means that LTB4 has a polyfunctional behaviour acting both as a chemoattractant and a sensitizer to other signals. Indeed, cells lacking the receptor for the primary chemoattractant fMLP (Formyl Peptide Receptor 1, FPR1) can still engage in directional migration in the presence of an fMLP gradient and fMLP-induced LTB4 secretion by WT cells. In contrast, for cells lacking the receptor for LTB4 ($Ltb4r1^{-/-}$), only those close to the wound engaged in chemotaxis while recruitment of those from distant sites was very inefficient. Other knockout and co-injection experiments confirmed the role of LTB4 paracrine signals in relaying the information of the primary chemoattractant to distant sites[27,29].

While many of molecular players involved in functional collective behaviour during wound healing have been identified, quantitative models of how this is accomplished through cellular interactions are still lacking. In the second part of this thesis, we develop a novel method to create hybrid cell-computer interfaces allowing for emulation of wound healing assays in which parameters of cellular communication can be quantitatively controlled.

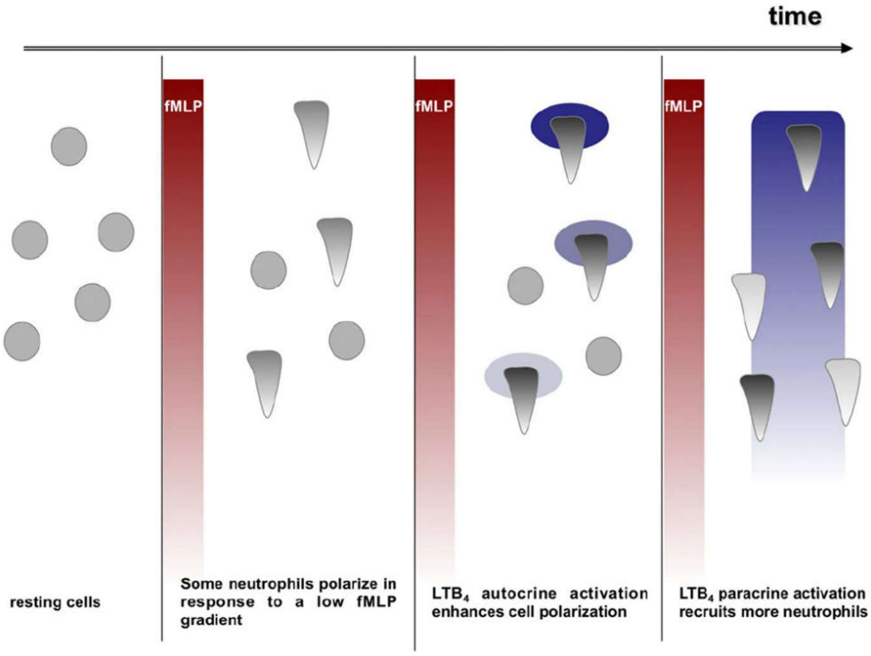

Figure 1.4: Scheme of chemotactic signaling-relay by secondary chemoattractant gradient formation in neutrophil chemotaxis

From left to right: in response to a primary chemoattractant gradient (fMLP, emanated from the wound site under physiological conditions), neutrophils secrete the chemoattractant LTB4 in an fMLP-concentration dependent manner. These paracrine and autocrine signals then form a secondary gradient of LTB4, which was found to also increase the sensitivity of cells to fMLP gradients, by facilitating polarization in the direction of the fMLP gradient. Overall, this results in recruitment of more neutrophils from regions where the fMLP gradient is low. Reprinted from [29] with permission from Elsevier, Copyright © 2012).

1.6 Observability and perturbation of collective behaviour

1.6.1 Cell shape and morphodynamic analysis

The mechanisms discussed above show that cellular morphogenesis results from the complex interaction of multiple processes, which are already complex dynamical processes themselves. Namely, cells have to detect extracellular morphogen gradients via receptors at the membrane, most likely in the presence of other signals and environmental noise, cells then engage the actuation of signal transduction networks, transduce this information to the dynamic cytoskeleton, extract the directionality of the signal, and finally integrate their current state with the perceived environment to generate a shape. This raises the question: which are the relevant observables to study how cellular morphogenesis arises from the interacting subsystems. Depending on the aspect of the system to be studied, different and specific observables would need to be chosen. However, because cell shape is the product of all these processes, cell shape constitutes a rich, informative observable that contains information of the internal cellular state. Indeed, already early on, when light microscopy enabled observation of individual cells, visual inspection of cell morphology started to play a major role in biology. "Phenotype" was directly associated with cell shape. In the last decades, however, advanced imaging techniques allow observation of cell shape with high spatiotemporal resolution and therefore quantitative morphometric analysis tools have been developed. Much of these efforts are directed to finding meaningful shape descriptors that are relevant to biological processes such as proliferation, migration and differentiation[30,31]. For example, automated analysis of morphometric parameters was used to discriminate erythrocyte morphologies[32]. Also, shape phenotypic variability in fish keratocytes was exploited to develop a model that quantitatively explains the relation between migration speed and cell morphology[33].

Crucially, beyond classification of static shapes, the dynamics of cell shape can be exploited to extract information of the dynamical processes underlying morphogenesis. In fact, in the past decades, morphodynamic analysis methods have been developed to understand the relation of signaling pathways to protrusion activity[34,35]. By identifying the contour of the cells, protrusion/retraction rates can be obtained from the contour evolution. This has been used to address the role of molecular players in the formation of distinct types of protrusions, known as lamellipodia[36] and filopodia[37], as well as cytoskeleton induced forces[38]. An even more powerful approach has been taken in recent studies, which related morphodynamic features to signaling activity of different RhoGTPases. This allowed investigation of how their activity is spatio-temporally coordinated both in the absence of cell stimulation[39], as well as during reorientation of neutrophil chemotaxis in response to a changing chemoattractant gradient[40]. Taken together, these insights establish that cell shape dynamics is a relevant observable to uncover mechanisms underlying morphogenesis.

1.6.2 Optogenetic tools

Of equal importance as the choice of relevant observables, is the interrogation of dynamical systems by perturbation. In this sense, the control of protein activity and localization by light has been a ground breaking advance in the study of cellular physiology. The use of optogenetic tools is now ubiquitous in biology due to the possibility to modulate protein function with high spatio-temporal control.

One of the modalities to accomplish modulation of protein activity is the use optical dimerizers to induce changes in the subcellular localization of proteins, such as kinases and MT-regulating effectors. One of the binding partners is anchored to a specific cellular localization, for example the plasma membrane, by means of targeting modules such as lipids or protein domains. In the absence of light, the complementary binding partner remains in the cytosol and upon light irradiation it translocates to the desired localization. Multiple light-sensitive proteins have been engineered to accomplish dimerization by light. Each variant differs in the spatial and temporal control that can be achieved, as well as the basal levels of binding in the dark and further oligomerization[41,42].

Recently, an improved Light-Induced Dimer (iLID) was developed which exhibits high spatial and temporal control as compared to some of the other variants[43]. The bacterial SsrA peptide was introduced on the C-terminal helix of the Light Oxygen Voltage 2 (LOV2) domain of *Avena sativa*. In the absence of blue light irradiation the SsrA peptide cannot bind its interaction partner SspB due to a steric block. Upon irradiation with blue light, the C-terminal helix in the LOV2 domain dissociates the protein enabling the interaction. The iLID tool has been combined with guanine nucleotide exchange factors (GEFs) like ITSN and Tiam1, such that upon blue light irradiation, the GEFs translocate to the plasma membrane. This translocation activates GTPase signaling, thereby inducing local changes in cell morphology such as lamellipodial protrusions and ruffling at the site of activation.

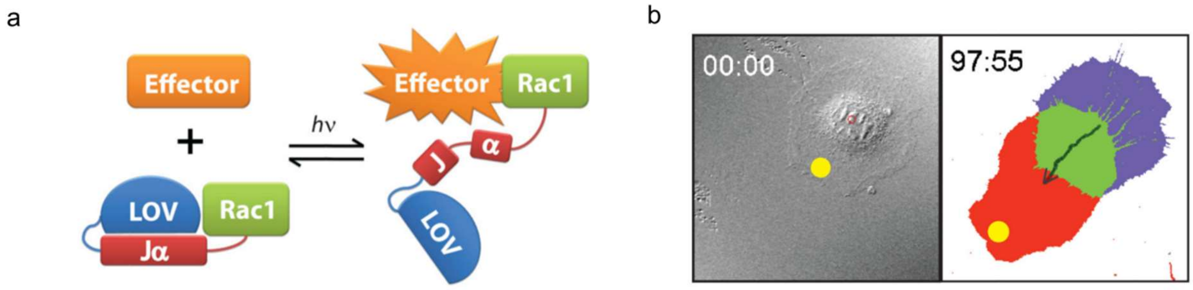

Figure 1.5: Photoactivatable Rac1

(a) Scheme of Photoactivatable Rac1 mode of action. Rac1 is fused to a LOV domain in such a way that it sterically blocks interaction with effectors, such as PAK1. In the presence of blue light, a conformational change leads to unfolding and dissociation of a Jα helix which links Rac1 and the LOV domain, releasing the steric block and allowing interaction with effectors. (b) PA-Rac1 induced migration of a MEF cell expressing PA-Rac1. Activation region denoted by yellow area. Time in minutes. (Reprinted from [44] with permission. Copyright © 2009, Springer Nature)

Another strategy for modulation of protein activity is the use of light sensitive domains fused to the protein of interest itself. This is the case of the Photo-Activatable Rac1 (PA-Rac1) protein, which was developed based on the Light Oxygen Voltage (LOV) domain from phototropin. Rac1 was fused to a LOV domain in such a way that it sterically blocks interaction with effectors in the absence of light (Figure 1.5a). In the presence of blue light, a conformational change leads to unfolding and dissociation of a Jα helix which links Rac1 and the LOV domain, releasing the steric block. It was shown that photoactivation of PA-Rac1 was sufficient to create lamellipodial protrusions and induce short range directional migration, in the order of half a cell size (Figure 1.5b).

1.6.3 Closed-loop optogenetics

Optogenetic tools as described above are generally used to produce acute perturbations through a fixed optogenetic input. However, a fixed stimulation procedure can lead to different responses in different cells. On the one hand, cells will express different levels of the optogenetic components, and thus the same light stimulation will lead to different activities. At the same time, for each cell, the relationship between light input and signaling activity may be also variable, and highly non-linear. Therefore, in a few studies, optogenetic tools have also been used as actuators for feedback control of cellular activity. For example, in the context of gene expression in yeast, optogenetic feedback control was implemented to reach user defined expression levels, strongly reducing cell-to-cell variability[45,46]. This was accomplished by dynamically adapting light induction of gene expression, from real time measurements of a fluorescence reporter. A similar strategy was implemented to deliver precise temporally varying signals to mammalian cells[47] (Figure 1.6a). To actuate the system, an optical dimerizer was used to translocate the phosphoinositide 3-kinase (PI3K) to the plasma membrane. This translocation induces the conversion of PIP_2 (phosphatidylinositol (4,5)-bisphosphate) into PIP_3 (phosphatidylinositol (3,4,5)-trisphosphate). As a readout, the production of PIP_3 was monitored in real-time through a PIP_3 sensor, namely, plasma membrane recruitment of the fluorescently labeled Pleckstrin homology domain (PH domain) of Akt. Therefore, pre-defined temporal profiles of PIP3 were generated in singles cells by adapting light inputs in real time through a feedback controller. This method was also applied to clamp levels of upon inhibition of its production with the PI3K inhibitor LY294002 (Figure 1.6b,c).

These feedback control methods differ from acute perturbations in that the dynamics of the system has to be taken into account to produce a desired cellular state. This is in strong contrast with traditional methods such as gene knockdowns, knockouts and small molecule inhibitors. These methods can reveal the presence of feedbacks within cells, but do not directly interrogate which type of dynamics underlies these feedbacks. However, a recent study combined optogenetic feedback control with genetic mutations to reveal the specific feedback dynamics of regulator molecules in yeast[48]. For this, the response to external pheromone stimuli was monitored when a component was knocked out. This response was compensated "on the fly" to match that of the wild-type, by calculating and delivering optogenetic inputs in real time. Examination of the compensation revealed distinct dynamic features for three known feedback regulators. All these approaches, indicate that hybrid experimental methods, in which cellular behaviour is interfaced with computers, may allow for a more successful recursion between experimentation and theory, in the investigation of molecular collective behaviour.

At a higher scale, an approach similar to the one proposed in this thesis was very recently applied in the context of gene expression pattern formation in yeast cells[49]. Instead of using closed-loop optogenetics to control cellular behaviour, it was utilized to emulate cell-to-cell signaling among yeast cells. The approach was inspired on human-in-the-loop strategies, where a human is made to interact with a simulation, for example in flight or driving simulators. This has the advantage of incorporating real human behaviour to the simulation, rather than modeling it, which will most likely not account for the relevant complex dynamics. In the "cell-in-the-loop" setup, real-time measurements of gene expression are used as inputs for a simulation of cellular interactions. From this simulation, light stimulus are calculated in real time and delivered to cells, forming a closed-loop dynamics. In this study, cells were assigned to patches on a virtual grid, while *in silico* interactions among living cells were programmed to laterally inhibit gene expression of neighbor patches. Once the signaling interactions and the virtual spatial arrangement are set, light stimulus are calculated based on the measurements, and the system evolves without any external control. Under certain parameters, the system exhibited spontaneous spatial patterning in the form of persistent checkboard patterns of gene expression. The advantage of this technique is that it allows to retain the natural behaviour of cells, while putting under computational control the parameters of the interaction.

The methods described in this section form the basis for the novel approach developed in the second part of this thesis. Rather than seeking control in the readout variable, we develop a cell-computer interface that allows for hybrid *in silico*-*in vitro* experiments to better investigate the collective behaviour of living cells, exemplified in the context of wound healing.

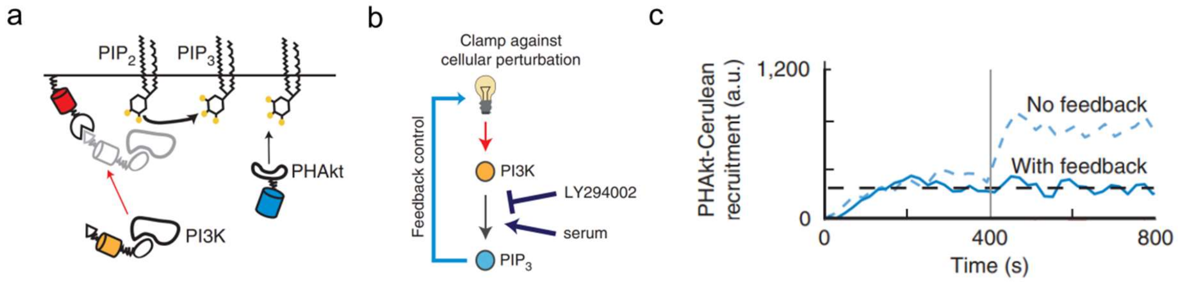

Figure 1.6: Optogenetic feedback control

(a) Translocation of PI3K kinase to the plasma membrane by means of an optical dimerizer constitutes actuation of the system, while readout for the feedback control is plasma membrane recruitment of the fluorescently labelled Pleckstrin homology domain (PH domain) of Akt (PH-Akt). (b) Scheme of feedback control for robustness of PIP_3 against inhibition or activation with small molecule inhibitors or serum, respectively. (c) PIP_3 levels as measured by PH-Akt recruitment before (t<400 s) and after (t>400s) inhibition of PI3K, with and without feedback control. (Reprinted/adapted by permission from Springer Nature: [47], Copyright © 2011)

1.7 Objectives

To date, many of the molecular players involved in morphogenesis and cytoskeletal reorganization have been identified. However, it remains unclear a) how morphologies arise from the bi-directional interaction between the cytoskeleton and signaling activity, b) how these interactions allow for memory of past morphogen patterns and c) how they determine subsequent signal-induced response. In the first part of this thesis, we address this by investigating the morphodynamics of reconstituted proto-cells. This synthetic morphogenic membrane system (SynMMS) is composed of an encapsulated dynamic microtubule (MT) aster together with a light-inducible signal transduction system in cell-sized liposomes. We set out to develop morphometric analysis methods, to understand:

1) how MT-induced deformations of the membrane arise and are stabilized, and therefore how is astral MT behaviour coordinated. For this we will develop local curvature kymographs to follow protrusion dynamics, 3D morphometric analysis to classify shapes, as well as image processing algorithms to enhance the visibility of astral MTs, and

2) how stable morphologies arise and what mechanisms underlie their plasticity or robustness to external global and local light cues. For this, we will develop approaches to determine relevant biochemical parameters, such as translocation of the signaling systems' kinase to the liposome membrane and the density of astral MTs. We will then relate them to the liposome morphodynamics.

At the same time, communication of such internal processing networks through intercellular signaling allows for coordinated behaviour in higher scale functions. Although many molecular players involved in cellular collective behaviour have been identified, it remains challenging to quantitatively investigate how a collective level dynamics arises from the communicating cells. Even across fields, this is because the investigation methods used are not systemic but rather molecular interrogations, namely, genetic modifications and acute molecular stimulations. Simultaneously, many bottom-up reconstitution approaches aim at elucidating such open questions by creating synthetic cell-like systems capable of communicating via diffusing molecules, or synthetic cell to cell contacts[50,51]. Although this greatly benefits from the component simplicity of synthetic systems, it is still hard to quantitatively control important variables such as the spatial arrangement of the communicating entities and more importantly, parameters of the interaction itself, making it challenging to understand how collective behaviour emerges.

In the second part of this thesis, we will create a hybrid cell-computer interface platform that enables virtual communication of living cells by optogenetic emulation of external signaling cues. We will exemplify the method in the context of wound healing. For this, we will first develop an automated microscopy platform to optogenetically direct mammalian cell migration. Then, we will develop a model of neutrophil recruitment to focal injury sites, based on previous experimental observations from the literature. This model will be used to investigate the conditions under which the recruitment radius is extended via paracrine signaling. Finally, we will integrate simulated intercellular signaling with the migration control platform, to create hybrid wound healing assays, where living cells migrate towards a virtual wound and virtually communicate in real time.

2 MATERIALS AND METHODS

2.1 Morphometric analysis

2.1.1 Centrosome Position and Eccentricity

A mask of the GUVs was obtained by thresholding the fluorescence intensity of fluorescently labeled tubulin at the plane of the centrosome and an ellipse was fitted to the mask in ImageJ. The centrosome position relative to the center of mask was calculated by:

$$Relative\ Centrosome\ Position = \frac{\left|\bar{r}_c - \bar{r}_{guv}\right|}{R_{guv}}$$

where $\bar{r}_c = (x_c, y_c)$ and $\bar{r}_{guv} = \left(x_{guv}, y_{guv}\right)$ are the position of the centrosome and the geometric center of the fitted ellipse obtained in ImageJ, respectively, and $R_{guv} = (M + m)/4$ where M and m are the major and minor axis of the ellipse. The eccentricity of the fitted ellipse was calculated as:

$$e = \sqrt{1 - \frac{m^2}{M^2}}$$

2.1.2 Curvature maps

At each time point of the time-lapse experiments, a mask of the GUV shape was made in the fluorescence image of labeled tubulin by performing a 2-pixel Mean Filter and thresholding in Fiji. Masks and CLSM images were imported to MATLAB 2018b. The points at the edge of the mask were ordered by their angle with respect to the geometric center of the GUV mask. The curvature was calculated using a custom made script which makes use of the function LineCurvature2D written by D. Kroon (University of Twente, August 2011) and available at the MathWorks File Exchange. The curvature at a point was calculated by considering as left and right neighboring points those which were 5 points away from it. The distance to the neighboring points determines how local the curvature is determined and was matched to allow visualization of MT-induced protrusions minimizing pixel noise. The curvature values were then binned into 130 angular bins for each time-point and the resulting matrix was plotted using the MATLAB function *imagesc*.

In order to further relate how the movement of the centrosome is coupled to the protruding activity, the maps were overlaid with a hollow black circle at each time column. The size of the circle represents the proximity to the membrane, the smaller the circle, the more central the positioning of the centrosome, while the bigger the circle, the closer the centrosome is to the membrane. A centrosome angular position can also be defined with respect to the center of geometry of the GUV. For example, in a polar morphology the centrosome will be located 180° away from the main protrusion. Thus, we set the location on the curvature map as the angle which is 180° away from the centrosome angle, so that in polar morphologies the centrosome and the protrusion overlap.

2.1.3 Fluorescence intensity angular maps

For the Alexa488-SspB-AuroraB (SspB-AuroraB^{488}) fluorescence intensity kymographs, the GUV mask at each time point was eroded and dilated using *imerode* and *imdilate* respectively, forming a 7 pixel band following the shape of the GUV. The mask was segmented into 230 angular bins, and the maximum intensity at each of them was taken.

2.1.4 Morphometric Classification

A 3D mask of the GUV shape was made in the fluorescently labeled tubulin confocal Z-stack, by performing a 2-pixel Mean Filter and thresholding. Masks were imported to MATLAB 2018b. The centrosome position was calculated as above, except that in 3D, $R_{guv} = (PA1 + PA2 + PA3)/6$ where $PA1,2,3$ are the Principal Axis Lengths and $\bar{r_c}$ is the GUV solid mask centroid. These were obtained by applying the in-built function *regionprops3* to the GUV solid mask. The diameter D of the minimal bounding sphere was calculated using the *minboundsphere* function by John D'Errico available at the MathWorks File Exchange. The diameter of the minimal inbound sphere was calculated by taking the maximum of the distance transform of the points contained in the GUV mask, to the GUV surface (edge of the mask) by means of the in-built function *bwdist*.

2.1.5 Quantification of AuroraB membrane translocation

Binary masks of the GUVs were obtained for the fluorescence intensity image of Tubulin (Alexa647-Tubulin) by thresholding in ImageJ as described above. The pixels corresponding to the membrane were defined as those 7 pixels away from the edge of the mask. This was obtained by eroding the mask by 7 pixels. Since the optical resolution was about an order of magnitude above the width of a lipid membrane, the fluorescence signal at membrane pixels contains contributions from both luminal as well as membrane located SspB-AuroraB^{488}. To correct for the luminal fraction contribution, the Tubulin channel was used as a reference. The fluorescence contribution of luminal SspB-AuroraB^{488} can thus be estimated as

$$AurB_{lum}\frac{Tub_{mem}}{Tub_{lum}} = AuB_{lum} * \varepsilon$$

Where $\mathrm{Tub_{mem}}$ and $\mathrm{Tub_{lum}}$ are the average fluorescence intensities of the Alexa647-Tubulin channel at the membrane pixels and the lumen pixels, respectively, while $\mathrm{AurB_{lum}}$ is the average fluorescence intensity of the SspB-AuroraB^{488} channel.

The amount of translocation relative to the lumen was then calculated as

$$R(t) = \frac{AuB_{mem}(t) * (1 - \varepsilon(t))}{AuB_{lum}(t)}$$

This operation can also be performed on a pixel basis, yielding images of $R(x, y, t)$, which we term translocation images of SspB-AuroraB^{488}. The analysis was performed using custom written code in MATLAB 2019b.

2.1.6 Quantification of nucleation strength by relative centrosome surface

A two-dimensional gaussian function was fitted to the fluorescence intensity image of the centrosome (from Alexa647-Tubulin) at the z-stack plane where the centrosome fluorescence intensity was maximal. The function followed the form

$$I(x, y) \ = \ B_1 + B_2 * e^{-\left[\frac{(x-x_0)^2}{2\sigma_x^2} + \frac{(y-y_0)^2}{2\sigma_y^2}\right]}$$

The centrosome size was then estimated as the area of the ellipse of axis lengths of σ_x and σ_y, normalized by the area spanned by the GUV at the same plane. In the case multiple nucleation centers were observed, which were close together but did not form a single peak, the same fit was performed for each of them and their respective normalized areas were added. The obtained number was scaled by a factor 100 for convenience. The analysis was performed with custom made code in MATLAB 2019b.

2.1.7 Enhancement of microtubule visibility

The visibility of the MT bundles in the Tubulin^{647} images was limited by the high background signal from free tubulin. The signal of MT bundles with respect to the background on the Tubulin^{647} fluorescence images was enhanced in Fiji with a custom made macro. First, contrast enhancement was applied ("Enhance Contrast", 0.3% of saturated pixels). Then, two consecutive directional filters were applied (MorphoLibJ library, Type=Max, Operation=Mean, Direction=32, Line=3 and Line=20, respectively), which are commonly used for enhancement of thin curvilinear structures. This was followed by an unsharp mask (Radius = 5 pixels, Mask Weight = 0.5). Lastly, the resulting image with enhanced curvilinear structures was multiplied by the original image.

2.1.8 Relative Centrosome Displacement

Centrosome position was quantified as in 2.1.1. The Relative Centrosome Displacement is then calculated as the absolute difference to first time point of activation.

2.2 Hybrid cell-computer interfaces

2.2.1 Plasmids

pTriEx-mCherry-PA-Rac1 was obtained from Addgene (Plasmid #22027) and used for transient transfection of MEF cells. For a stable cell line with doxycycline inducible expression, mCherry-PA-Rac1 was cloned into the back bone of the PB-TET-mcMyc (Addgene Plasmid #22027) by replacing the mcMyc insert with mCherry-PA-Rac1.

2.2.2 Cell culture

MEF cells (CRL-2752, ATCC) were grown in Dulbecco's modified Eagle's medium (DMEM, PAN Biotech) supplemented with 10% fetal bovine serum (FBS, PAN Biotech), 2 mM L-glutamine, and 1% nonessential amino acids (NEAAs, PAN Biotech) and maintained at 37°C in 5% CO2. When required, cells were transfected 24 hours before the experiment using Lipofectamine 2000 (Life Technologies) according to the manufacturer's protocol. For the experiments involving virtual communications among cells, a the stable cell line with inducible mCherry-PA-Rac1 expression was used. This was done to minimize the presence of dead cells associated with transient transfection, which could obstruct the movement of the photoactivated migrating cells. For the stable cell line, cells were first transfected with the PB-TET-mCherry-PA-Rac1, and put cells under selection pressure for 14 days at 750 ng/ml of Neomycin (G418).

2.2.3 Cell preparation for live-cell experiments

For the live-cell experiments, MEFs were seeded onto fibronectin-coated (1.85 ug/cm^2; F0895, Sigma Aldrich) four-well chambered glass slides (Lab-Tek, Nunc), at density of 2000 cells per well. Cells were either transiently transfected as described above 24 hours before the experiment, or in the case of the stable mCherry-PA-Rac1 cell line, induced with 500 ng/ml of doxycycline hyclate (D9891, Sigma Aldrich) 24 hours before the experiment. One hour before the start of the experiment, the complete growth media was replenished.

2.2.4 Fluorescence Imaging and Photoactivation

The fluorescence of cells expressing PA-Rac1-mCherry was imaged using a custom built microscope based on an Olympus IX81 body (Olympus Life Science Europa), equipped with a temperature and CO_2 controlled stage top incubation chamber set at 37°C and 5% CO_2 (tempcontrol 37-2 digital, Heating Insert P, CO2-Controller, CO_2 Cover HP 347, all from PeCon Gmbh, Germany). For illumination of localized regions, a Mosaic3 Duet (Andor Technology) was connected to the back port of the microscope body, and a pE-4000 (CoolLED) was used as light source connected to the Mosaic3. For photoactivation, the 435 nm LED at 25% power (1.8 mW at the objective focal plane) was selected, while for mCherry excitation the 580 nm LED was used at 50% power (1.1 mW at the objective focal plane). Excitation spectra was restricted by a fluorescence filter placed at the pE4000 Channel C slot for filters (Brightline Fluorescence Filter 575/15, Semrock). The fluorescence filter cube contained a dual band beamsplitter (59022bs, Chroma Technology) and a dual band emission filter (59022m, Chroma Technology). Detection of mCherry fluorescence emission was restricted with a bandpass filter (609/54, FF01-609/54-25, Semrock). For photoactivation the exposure was set to 500 ms, as well as 500 ms for mCherry imaging. Transmission images were also taken to verify that non-fluorescent cells were not in contact with the stimulated cells. The exposure time was 250 ms and shorter wavelengths of the lamp were filtered with a longpass filter (SCHOTT OG590-45M3, AHF Analysentechnik AG). The microscope control was programmed in MicroManager 1.4, through its interface with MATLAB 2019b, using custom made code.

2.2.5 Real-time tracking and photoactivation for PA-Rac1 induced migration

First, a stage position with a cell expressing PA-Rac1-mCherry is selected. A transmission snapshot is taken to verify the cell is neither in contact nor closely neighbored by other non-fluorescent cells. A square around the cell is drawn by the user at the begging of the experiment, and a binary cell mask is obtained by performing background subtraction and triangle thresholding. The mask is smoothed by applying subsequent erosion and dilation. To target cells to a specific point in space, the user selects a target point within the image. The vector between each point in the mask and the target point is calculated, and projected into the vector joining the center of geometry of the mask and the target point. The magnitudes of these vectors are normalized to its maximum and minimum. The mask for photoactivation is then defined by the points with a value greater than 0.3, that is, defining the front 30% of the cell (this value was found to be sufficient for long range migration, although further optimization could be conducted). For subsequent frames, the tracking square is automatically repositioned to the center of the cell mask at the previous frame. The excitation mask is then uploaded to the Digital Micromirror Device (Mosaic3) and projected to the sample. In order to correctly target the part of the cell defined by the excitation mask, a calibration was performed to obtain a mapping between the Digital Micromirror Device pixels and camera pixels. For the calibration, a series of small disks (7 pixel diameter) arranged in a grid were sequentially projected to a mirror sample and the center of disk was retrieved from the camera image. From this, an affine transformation was calculated that maps the Micromirrors to the camera pixels.

2.2.6 Chemotactic index

The chemotactic index was calculated as the cosine between the velocity (taken between positions separated by 3 minutes) and the target direction. For Figure 4.2 and Figure 4.3 trajectories were first smoothed using a 9 point window Savitzky-Golay filter to reduce position noise.

2.2.7 Persistent Biased Random Walk (PBRW) simulations

Simulations were run in custom made code in MATLAB 2019b according to the equations described in section 4.3. The time step was set to be 1 unit, equivalent to 1 minute, and the space unit to 1 μm, in order the parallel the experiments. Parameters were set to: $A_w = 0.5 \times 10^{-5}$, $R_w = 20$, $\mathbf{x}_w = (0,0)$, $A_P = 10^{-9}$, $R_P = 30$, except when no paracrine signaling was present ($A_P = 0$), or when the dependence on parameters was studied, where the values are indicated in the corresponding figures. For the parameters of the OU see 2.2.8. Cells were arranged in three concentric rings having 4, 8 and 8 cells respectively. This was decided to parallel experiments, in which experimental conditions allowed for simultaneous control of around 20 living cells at the required frame rates for migration control. Separation between rings was chosen to be twice the average cell size (2x28μm). Initial position of cells was set at radiuses 126 μm, 182 μm, and 238 μm, respectively, spaced by equal angles at each ring. The average recruitment radius was calculated as $R = \sqrt{A/\pi}$ where A is the area of the supra-threshold region.

2.2.8 Estimation of PBRW parameters

We first obtained an estimation of the PBRW parameters in the absence of activation by fitting an expanded version of Fürth's formula as previously described[52] with the published MATLAB code, and obtained the values: D = 0.5, τ=36, and positional noise σ=1. To estimate the strength of the bias u, we compared simulations in which cells were imposed a bias in a fixed direction to experiments of unidirectional PA-Rac1 induced migration (Figure 4.2). We manually adjusted the bias strength to the average absolute traveled distance, to match the long term behaviour of the experimental data, obtaining a bias strength u=0.22 (see Eq. 3). These estimations could be improved by running a stochastic optimization.

2.2.9 Mapping of living cells position into virtual space

In order to map cells from positions in their individual images to a shared virtual space, a target direction point is first chosen in real space, z_t, in the pixel coordinates of the field of view. Then, the mapping between real and virtual space is constructed by rotating and translating the coordinates such that the given target direction corresponds to the direction of the vector between the initial position in virtual space Z_0 and the location of the virtual wound, in this case, (0,0). Then the mapping between real and virtual space is given by a rototranslation:

$$Z = Z_0 + (z - z_0)e^{i(\theta_{Z_0} + \pi - \theta_{E_{vec}})}$$

where $Z = X + iY$ is the virtual position of a cell expressed in the complex notation, Z_0 is the initial virtual position. Z_0 is defined by the user according to the desired arrangement of cells in virtual space. z is the center of the cell mask in pixel coordinates, thus $z_0 = z(t = 0)$ and θ_{z_0} is the angle of the vector z_0. $\theta_{E_{vec}}$ is the angle of the vector $E_{vec} = z_t - z_0$.

3 PART I: A SYNTHETIC MORPHOGENIC MEMBRANE SYSTEM THAT RESPONDS WITH SELF-ORGANIZED SHAPE CHANGES TO LOCAL LIGHT CUES

For this chapter, the author developed quantification methods and conducted data analysis for all the experiments presented, unless otherwise stated. Experiments and data acquisition were performed by K. Gavriljuk, F. Ghasemalizadeh and H. Seidel. For materials and methods regarding experiments we refer the reader to the following reference[16].

3.1 Design of the Synthetic Morphogenic Membrane System

To capture essential features of cellular information processing arising from morphogen induced changes in cell shape, the reconstituted proto-cells were designed to mimic the dimensionality reduction operational principles of the Rac1-Pak1-stathmin MT-regulator network (Figure 3.1). For this, an MT-aster system and a signaling system were encapsulated in giant unilamellar vesicles (GUVs). Molecular components were encapsulated by continuous droplet interface crossing encapsulation (cDICE)[16,53]. The MT-aster system was composed of purified centrosomes, purified tubulin and GTP, which were encapsulated in GUVs. For the signaling system, the light inducible dimer iLID was used, where SspB was fused to the stathmin kinase AuroraB. Upon blue light irradiation SspB-AuroraB translocates to the membrane bound C2-iLID, emulating morphogen-induced PAK translocation to the plasma membrane. Membrane recruitment of the stathmin kinase SspB-AuroraB, induces local stathmin phosphorylation at the morphogen exposed area leading to MT-growth. We refer to these proto-cells as a Synthetic Morphogenic Membrane System (SynMMS).

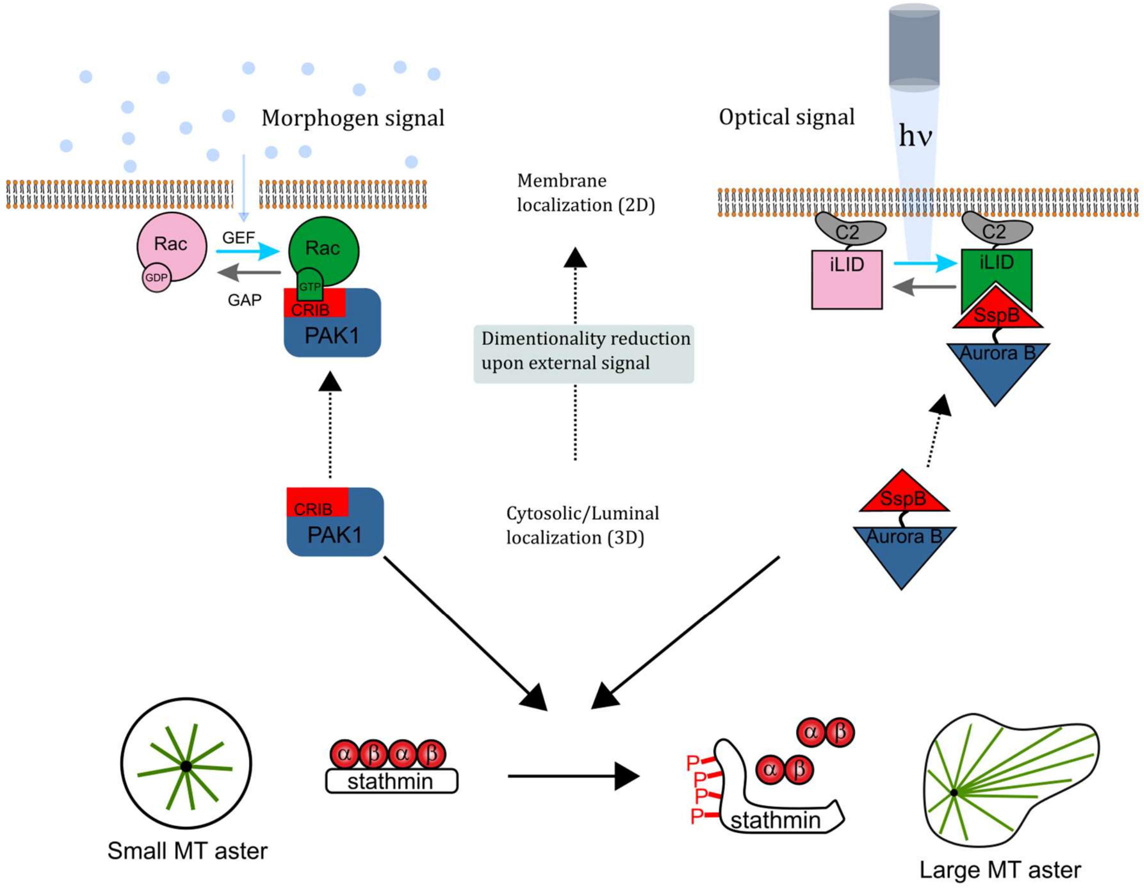

Figure 3.1: Synthetic transduction network mimics naturally occurring Rho-GTPase signal transduction to the cytoskeleton

Natural (left) and synthetic (right) signal transduction networks. Activation (vertical black arrows) of natural or synthetic signal transduction by translocation of PAK to Rac-GTP (via CRIB domain) or SspB-AuroraB to C2-iLID on the membrane (curved blue arrows). Upon local translocation of a stathmin kinase, phosphorylation of stathmin (horizontal black arrow) induces MT growth (green asters) by increasing the amount of available tubulin for polymerization. GEF: guanine nucleotide exchange factor, GAP: GTPase activating protein, Rac: small GTPase, PAK, AuroraB: serine threonine protein kinases, stathmin: MT regulator, iLID/SspB: improved light-inducible dimer and its binding partner, C2: phosphatidylserine binding domain. Scheme adapted from [16].

3.2 Dynamics and biochemical regulation of encapsulated MT-asters

3.2.1 Morphological states of an encapsulated MT-aster

We first investigated which morphologies arise from the encapsulation of tubulin with purified centrosomes. At tubulin concentrations of 15-25 μM, we found that most GUVs exhibited a round shape. The average MT length around the centrosome was smaller than the radius of the GUV, and the centrosome was positioned around the center of the GUV (Figure 3.2a). In order to quantify these observations, we calculated two magnitudes. First, to capture the global morphology, we calculate the eccentricity of the GUV at the observation plane. Second, we defined a magnitude to reflect the position of the centrosome relative to the GUV, which yields 0 at the center of the GUV and 1 when the centrosome is located at the membrane. (Methods, 2.1.1). Indeed, the quantification showed centrosome position values close to 0, and so did the eccentricity (Figure 3.2b). In contrast, when the encapsulated tubulin concentrations were in the range of 35-40 μM, we observed a richer set of morphologies. On the one hand, some GUVs showed a centrosome that was slightly displayed to the periphery with most of the microtubules directed to the opposite side. This morphology has been observed before and described as "semiaster", because the MTs of the aster are mostly on one side of the centrosome[54]. We also observed GUVs where most astral MTs had a length that exceed that of the GUV diameter, therefore curving along the membrane, leading to a cortical MT distribution. Yet another population was observed in which astral MTs were able to deform the membrane, forming a protrusion at the opposite site of the centrosome, defining a polarity axis. The differences in morphology were captured by the eccentricity, where a bimodal distribution was observed. GUVs with eccentricities of around 0.1 correspond to the cortical and semiaster morphologies, while the GUV points with higher eccentricity correspond to morphologies with one or more protrusions.

Next, we investigated whether it was possible to bias the observed states towards the polar morphology. For this, GUVs where formed under hyperosmotic conditions by increasing the concentration of glucose on the outside buffer (100 mOsm). Quantification of centrosome position and eccentricity confirmed this was the case, where the distributions shifted towards more peripherally positioned centrosomes and higher eccentricity values.

Taken together, this results show that 1) the configuration of the aster, understood as the length and angular distribution of the MTs at a given point in time, restricts the positions at which the centrosome can be and that 2) this configuration as well as the overall morphology, depend on the amount of encapsulated tubulin as well as the osmotic difference.

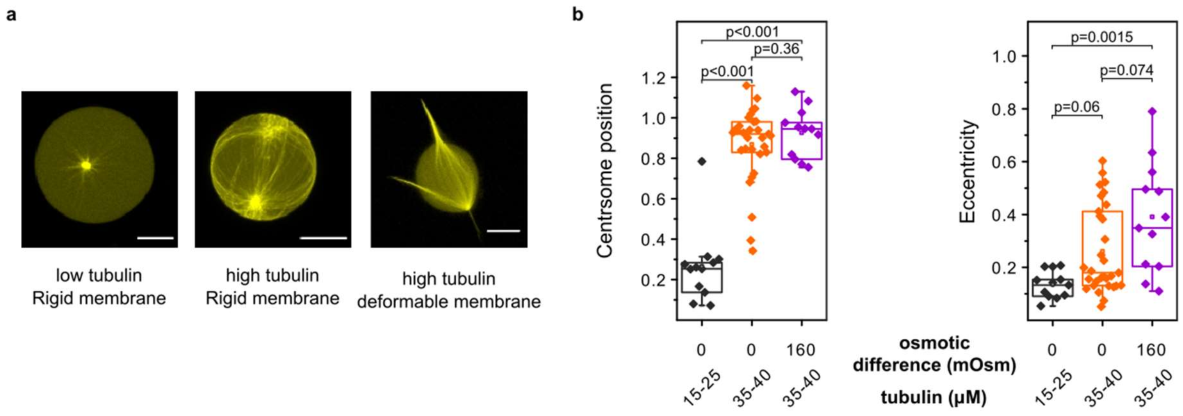

Figure 3.2: Self-organized morphologies of GUVs containing encapsulated MT-asters

(a) GUV morphologies, from left to right: small aster at low tubulin (15 – 25 µM), cortical aster and polar morphologies at high tubulin concentration (35 – 40 µM). Right GUV at lowered membrane tension (hyperosmotic surrounding solution). (b) Morphometric quantification of individual GUVs with high or lowered membrane tension, and low or high tubulin concentration. Centrosome position: 0 – centered, 1 – membrane proximal, eccentricity: 0 –perfect circle, >0 – deviations from circle. All p-values from two-sample Kolmogorov-Smirnov test. Scale bars 10 µm. Encapsulated MT-asters in GUVs were prepared and experiments were performed by F. Ghasemalizadeh. Analysis in (b) by B. Scocozza.

3.2.2 Local curvature kymographs

Although centrosome position and eccentricity capture features of the global morphology, they do not contain information about local events that occur at the membrane, such as the interaction of dynamically instable MTs with the membrane. Therefore, we set out to develop curvature maps, which allow us to follow the dynamics of the membrane, as a reflection of the interaction with membrane deforming MTs.

To this end, we processed the confocal images of fluorescently labeled tubulin to obtain a closed curve delineating the membrane. The curvature at each point of the curve can be then calculated by fitting a parabola to that point and two neighbouring points, one to the left and one to the right, at a certain boundary point separation. This parametrizes the boundary and therefore the curvature can be analytically calculated for each boundary point at each frame of the time-lapse (see section 2.1). The separation to the neighbouring points determines the locality of the metric. For example, when choosing neighbours too close by, ~1 pixel, pixel noise becomes very present. At the other extreme, the locality of the measure is lost. Therefore, by visual inspection, we chose the separation according to the imaging conditions used for the experiments, to maximize the locality and minimize the noise (see Methods 2.1).

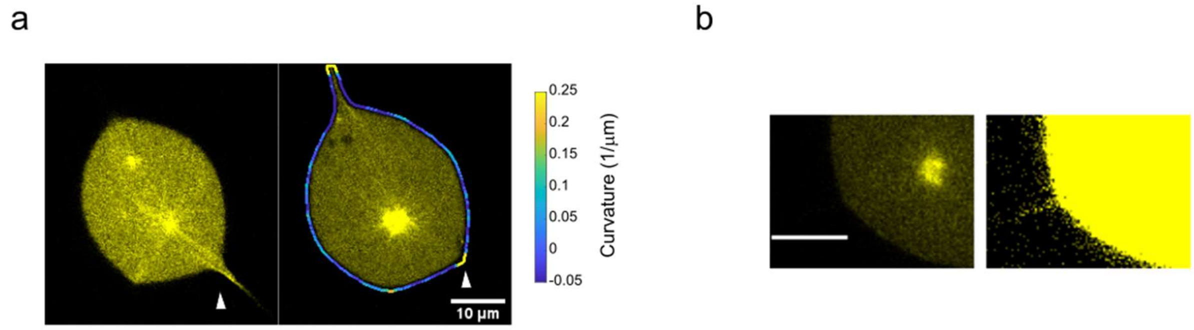

Figure 3.3: Local curvature of the GUV membrane
(a) Fluorescence images of fluorescently labeled tubulin in GUV with an encapsulated MT-aster at two different planes of a confocal z-stack. Right image is overlaid with GUV contour color-coded by local curvature at the observation plane. White arrow indicates a protrusion that is in focus at one plane (left) and not in focus at another plane (right), yet detectable by an increased membrane curvature. (b) Micrographs at low (left) or high (right) contrast, showing that out of focus protrusions can sometimes be detected when significantly enhancing the contrast. Scale bar: 10 µm.

In addition, it was not possible to acquire time-lapses of 3D z-stacks due to photobleaching and phototoxicity, so 2D time-lapses at the plane of the centrosome were acquired. Therefore, in some instances protrusions may not be in the plane of focus. However, protrusions bend the membrane over extended areas in their vicinity, meaning that protrusions themselves can be detected through this long-range deformation even when out-of-focus, which is reflected in the local curvature (Figure 3.3a). At the same time, out-of-focus protrusions may still yield an extremely dim, but measurable signal. This can be detected by observing the images at extremely high contrast levels. If the detectors are photon counting detectors, like for our experiments, this means observing the image in the range of few counts, even between 1 or 2 counts per pixel. Therefore, out-of-focus protrusions that are not apparent at first glance can be detected and delineated by the masking algorithm (Figure 3.3b). These maps are used to analyze and interpret the experiments in the next section and the following sections.

3.2.3 Self-induced capture underlies self-organized shapes of the encapsulated MT-aster

In order to investigate the dynamics that leads to the observed morphologies, experiments were conducted where MT-growth was induced by raising the temperature from 20°C to 34°C. This signal, is analogous to a spatially uniform morphogen signal which initiates MT growth. Under rigid membrane conditions, we observed that MT-growth resulted in strong decentering of the centrosome towards the periphery, giving rise to semiaster morphologies (Figure 3.4a). In contrast, in the presence of a deformable membrane, the initial morphology exhibited isotropically distributed protrusions, and temperature induced MT-growth evolved the morphology towards a polar protrusion morphology (Figure 3.4b). These could be observed in their respective curvature maps. The map remains flat for the rigid case, while in the deformable case we observed multiple peaks spanning all angles that evolve to two peaks in the final frames. In the transition to a polar morphology, multiple protrusion merging events could be observed in the local curvature kymographs.

These observations suggest that at the onset of polymerization, each growing MT contributes with a pushing force to the centrosome, where a random imbalance of the net force leads to displacement towards the periphery. The angle at which growing MTs encounter the membrane is biased by the displacement, resulting in a net force that not only further displaces the centrosome in the same direction, but also promotes gliding of the MT-induced protrusions along membrane towards the opposite side. Once this initial displacement takes place, the system engages a recursive processes of centrosome displacement and protrusion coalescence: as the centrosome decenters, protrusions merge and glide along the membrane towards the opposite site, to form a polar protrusion morphology.

The process of coalescence is consistent with the observation of multiple MTs bending into single protrusions in the stable morphologies shown in Figure 3.2. Essential to the correct understanding of this process, is to consider the intrinsic dynamic instability of MTs: by alternating between growth and schrinkage, MTs constantly sample the GUV lumen, including the membrane proximal region. When taking this into consideration, our observations suggest that stable MT-induced protrusions are created by “self-induced capture” (SIC, Figure 3.5). Initially, dynamic instability leads to small and transient membrane deformations, which form a capture site for neighbouring microtubules that further reinforce and stabilize the protrusion. As MTs get captured in the protrusions, depletion of “free” MTs occurs, implying future transient protrusions are much less likely to be stabilized than before. This means, that depletion itself, further contributes to stabilization of the shape. Altogether, these results show that the deformable membrane provides an indirect coupling between the astral MTs, which gives rise to collective MT behaviour resulting in a symmetry broken morphology with protrusions at the poles.

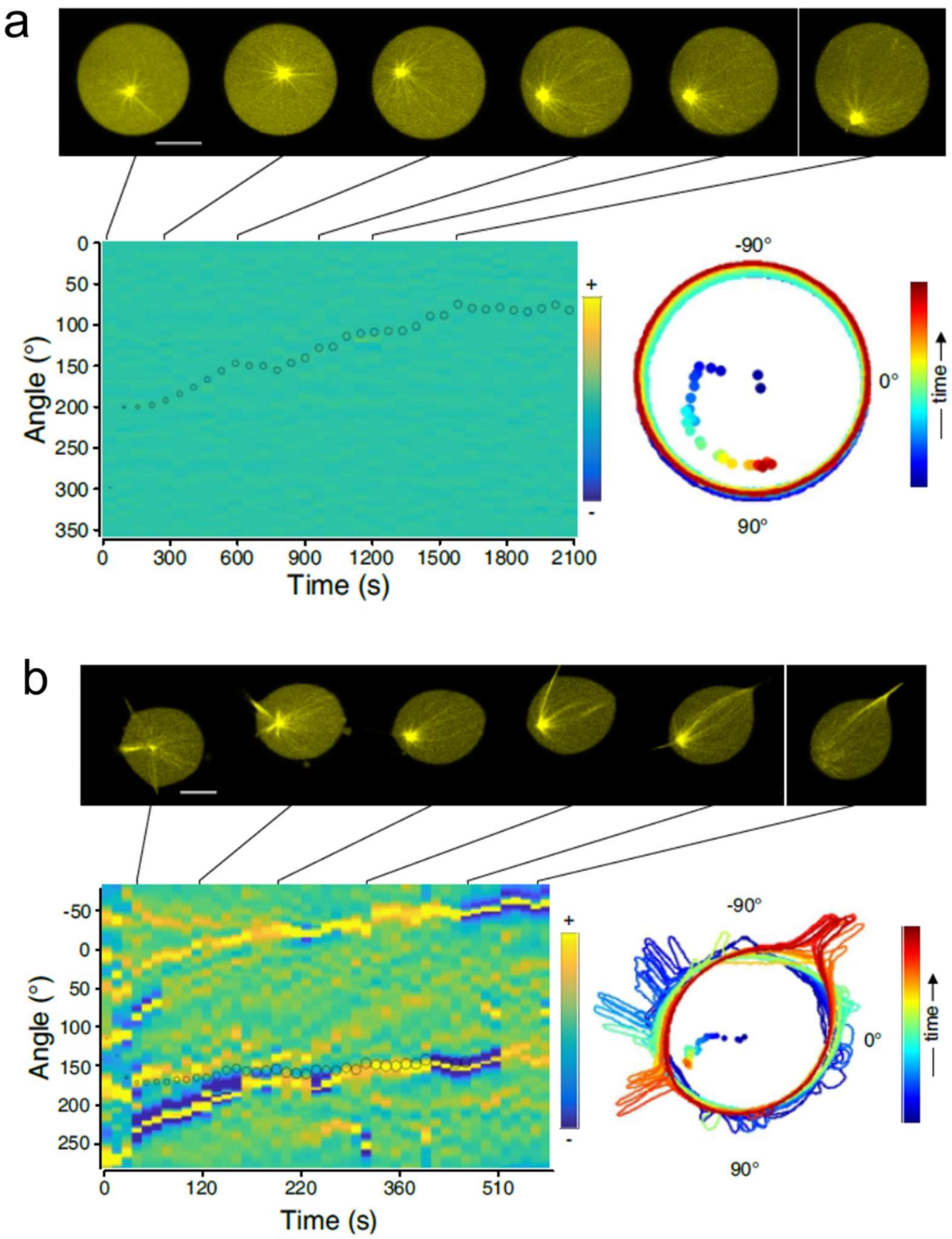

Figure 3.4: Visualization of microtubule-membrane interactions via curvature maps
(a) Top: time-lapse of temperature-induced aster growth in a GUV with high membrane tension. Bottom left: local membrane curvature kymograph (right: color code) overlaid with centrosome

position (small circle: central, large circle: peripheral). Bottom right: GUV contours color coded by time progression (dots: corresponding centrosome positions). (b)Time-lapse of temperature-induced aster growth in GUVs with low membrane tension. Representation as in (a). Encapsulated MT-asters in GUVs were prepared and experiments were performed by F. Ghasemalizadeh. Analysis by B. Scocozza.

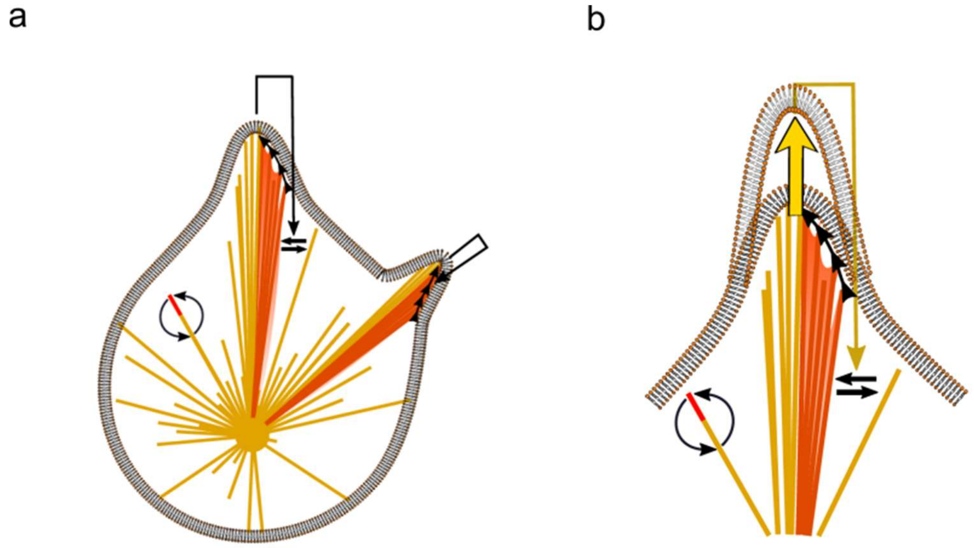

Figure 3.5: Self-induced capture mechanism underlies self-organized shapes of the encapsulated MT-aster

(a) Scheme of self-induced capture (SIC) protrusion formation. MT-induced membrane deformations promote further capture of neighboring MTs (straight arrows), which slide into the protrusion (arrow heads) thereby depleting free MTs. Curved arrows represent MT dynamic instability. (b) Enlargement of the scheme at a protrusion, depicting how capture of MTs leads to protrusion growth.

3.2.4 Phosphorylation state of stathmin regulates MT-aster-induced GUV morphology

In order to establish biochemical regulation of the encapsulated MT-aster system, the microtubule regulator molecule Stathmin (OP18) was introduced. The effect of stathmin on microtubule behavior was previously studied and characterized in the laboratory by K. Gavriljuk and F. Ghasemalizadeh[16]. Briefly stated, it was shown that unphosphorylated stathmin acts as a tubulin sequestration molecule, which diminishes the availability of tubulin heterodimers for polymerization. In contrast, upon phosphorylation, the affinity of one of the tubulin binding sites significantly decreases, diminishing the sequestration effect, increasing the available pool of polymerizable tubulin.

Therefore, experiments were performed to decide if stathmin regulation of the encapsulated MT-aster can be observed. Indeed, the morphometric quantification shows that when 5 µM stathmin were co encapsulated with 40 µM tubulin, we recapitulated the morphologies that were observed at lower tubulin concentrations, namely, round shapes with asters smaller than the GUV size. In contrast, in the presence of phosphorylated stathmin, the distributions shifted towards the polar morphologies, exhibiting a centrosome positioned at the periphery and higher eccentricities (Figure 3.6). These results indicate that the morphology of vesicles with encapsulated MT-asters can be controlled by a signaling system that phosphorylates stathmin.

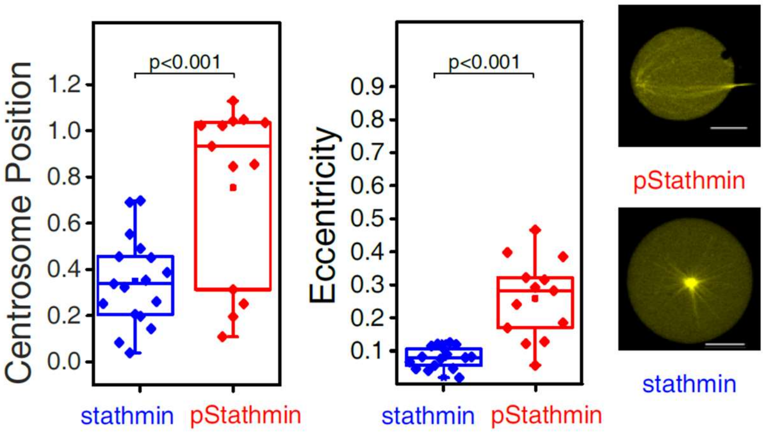

Figure 3.6: Effect of the MT regulator stathmin on GUV morphology

Morphometric quantification of individual GUVs with encapsulation of 5 µM stathmin or pStathmin (40 µM tubulin). Right: representative images. Centrosome position: 0 – centered, 1 – membrane proximal, eccentricity: 0 –perfect circle, >0 – deviations from circle. p-values from two-sample Kolmogorov-Smirnov test. Scale bars 10 µm. Encapsulated MT-asters in GUVs were prepared and experiments were performed by F. Ghasemalizadeh. Analysis by B. Scocozza.

3.3 Properties of a reconstituted signal transduction system

A biochemical signaling system that mimics morphogen induced signal transduction was developed in the laboratory by K. Gavriljuk[16]. The main features of this system are described below, some of which were analyzed with methods developed in this thesis.

3.3.1 An optical dimerizer system that mimics morphogen-induced dimensionality reduction

The signaling system was designed to mimic the transduction of environmental cues into regulators of the cytoskeleton. In particular, the system parallels the operational principle of the Rac1-Pak1-stathmin pathway, where an external signal induces translocation of GEF to the membrane. This reduction in dimensionality, from luminal 3D to membrane 2D, results in the activation of GTPases[26], such as Rac1, leading to phosphorylation of stathmin by Pak1[19–21]. In the synthetic system, the iLID/SspB optical dimerizer system[43] was encapsulated in GUVs, where iLID was associated to the membrane by a C2 phosphatidylserine-binding domain (C2-iLID) and SspB was fused to AuroraB kinase (SspB-AuroraB). Upon blue light irradiation, SspB-AuroraB translocated to the membrane (Figure 3.7a). We observed a fraction of SspB-AuroraB was located at the membrane, even before blue light irradiation, which we will refer to as basal translocation. Importantly, localized blue light irradiation resulted in a translocation gradient along the membrane (Figure 3.7b), showing that the system can mimic a spatially graded response as if originating from an extracellular morphogen gradient.

In order to analyse the stability of the translocation gradient along the membrane, we developed angular fluorescence intensity maps (see 2.1.3). These maps show the fluorescence intensity distribution along the membrane, as a function of the angle with respect to the center of geometry of the GUV. From the fluorescence map, we could visualize and quantify the spatial extent and the establishment dynamics of the translocation gradient. For this, we plotted fluorescence intensity evolution profiles at different distances from the irradiation center, as well as the angular profiles at several timepoints (Figure 3.7b). The extent and dynamics are dependent on a number of experimental factors: the diffusion of C2-iLID/SspB-AuroraB along the membrane, the binding kinetics of the optical dimerizer, and the irradiation dosage. We observe that under our experimental conditions[16], the gradient reaches a stable steady state in the order of 50 seconds, and decays ~3% per micrometer along the membrane. After release of blue light irradiation, the C2-iLID reverts to its closed conformation, where no SspB-AuroraB[542] can bind, leading to recovery of the luminal localization. This reversibility is of crucial importance since it allows us to expose the system to subsequent localized stimuli at different sites, as if originating from a changing morphogen environment. These results show that the optical dimerizer system can mimic morphogen induced translocation of kinases to the membrane as if originating from a local morphogen cue.

The SspB-AuroraB^{488} construct was used in all further experiments to avoid spectral crosstalk with tubulin^{647}. Therefore, 488 nm irradiation both activates the iLID and excites the fluorescence of Alexa488-SspB-AuroraB used for the observation of SspB-AuroraB translocation.

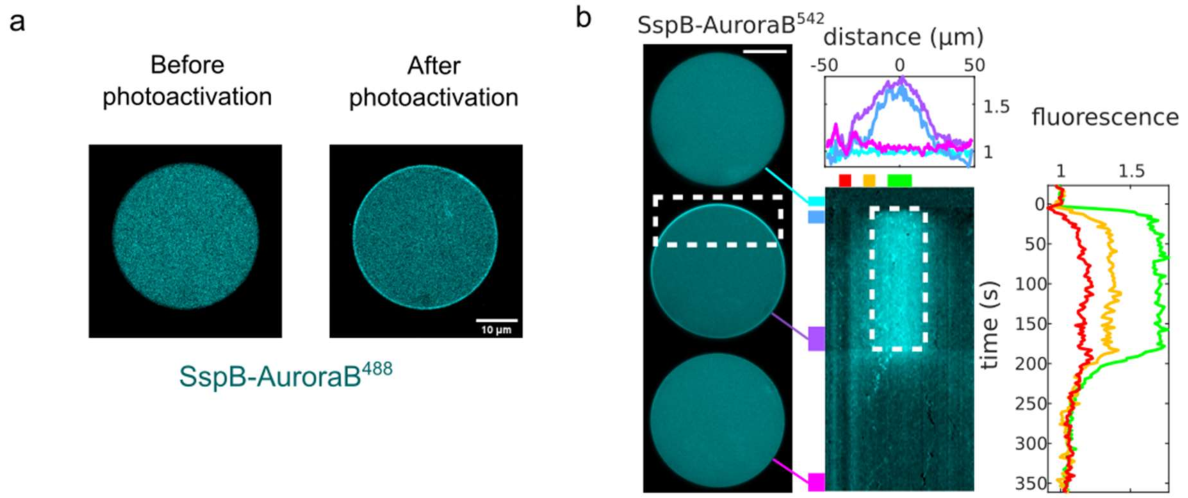

Figure 3.7: Light-induced SspB-AuroraB translocation to the GUV membrane
(a) Alexa488-SspB-Aurora images (cyan) before and after global blue light induced translocation to the membrane associated C2-iLID. (b) GUV with encapsulated C2-iLID and SspB-AuroraB^{542} upon local irradiation. Left: averaged frames from times indicated by cyan-to-magenta boxes connected with lines to the kymograph of SspB-AuroraB^{542} fluorescence (middle). X-axis: distance along membrane from the the 12 o'clock position; y-axis: time, dashed boxes: 488nm-irradiated duration/position. Profiles top and right of kymograph from averaged time/space frames marked by colored boxes (cyan-to-magenta: time, green-to-red: space). Fluorescence normalized to average intensity per frame. Scale bars 10 µm. GUVs were prepared and experiments were performed by F. Ghasemalizadeh. Analysis by M. Schmick.

3.3.2 Stathmin phosphorylation gradient

Next, the translocation system was co-encapsulated together with stathmin to couple kinase translocation to modulation of tubulin sequestration. In the absence of translocation, we expect a fraction of stathmin to be phosphorylated at steady state, uniformly across the GUV. Upon translocation, the effective activity per volume element is spatially rebalanced, biasing phosphorylation activity towards the membrane proximal region, while diminishing activity in the lumen. However, if the spontaneous back conversion from pStath to unphosphorylated stathmin is negligible, diffusion will homogenize this imbalance, leading to a uniform fraction of pStath. Hence, the phosphatase λ (PPλ) is introduced to counter the activity of the kinase. In the presence of both enzymes, a reaction cycle is established. Before translocation, the system remains mostly unphosphorylated due to the high PPλ intrinsic activity over the AuroraB activity. Upon translocation, however, this cycle is rebalanced, leading to a dominating kinase activity at the membrane proximal region and a phosphatase dominated cycle in the lumen. Thus, the ensuing spatial cycle imbalance leads to a gradient of phosphorylated stathmin emanating from the membrane.

Through a thorough biochemical characterization[16], the system was therefore set to such conditions and the results of experiments showing the stathmin phosphorylation gradient are shown in Figure 3.8. A conformational FRET sensor was used to image stathmin phosphorylation states. As expected, in the absence of PPλ, no phosphorylation gradient was observed upon translocation, while and in the presence of PPλ a steep gradient from the GUV membrane was measured.

We found that a direct consequence of the stathmin phosphorylation gradient is an enhanced tubulin concentration maintained near the membrane. The high kinase activity at the membrane lowers the concentration of unphosphorylated stathmin, creating a negative gradient. Therefore, the net diffusional flux of tubulin bound stathmin is towards the membrane where AuroraB kinase phosphorylation releases tubulin from stathmin. Phosphorylated stathmin diffuses towards the lumen where it is dephosphorylated by luminal PPλ, enabling rebinding of tubulin hetero-dimers, closing the ATP driven tubulin deposition cycle. Therefore, this spatially imbalanced reaction cycles can be conceptualized as a “molecular tubulin pump”.

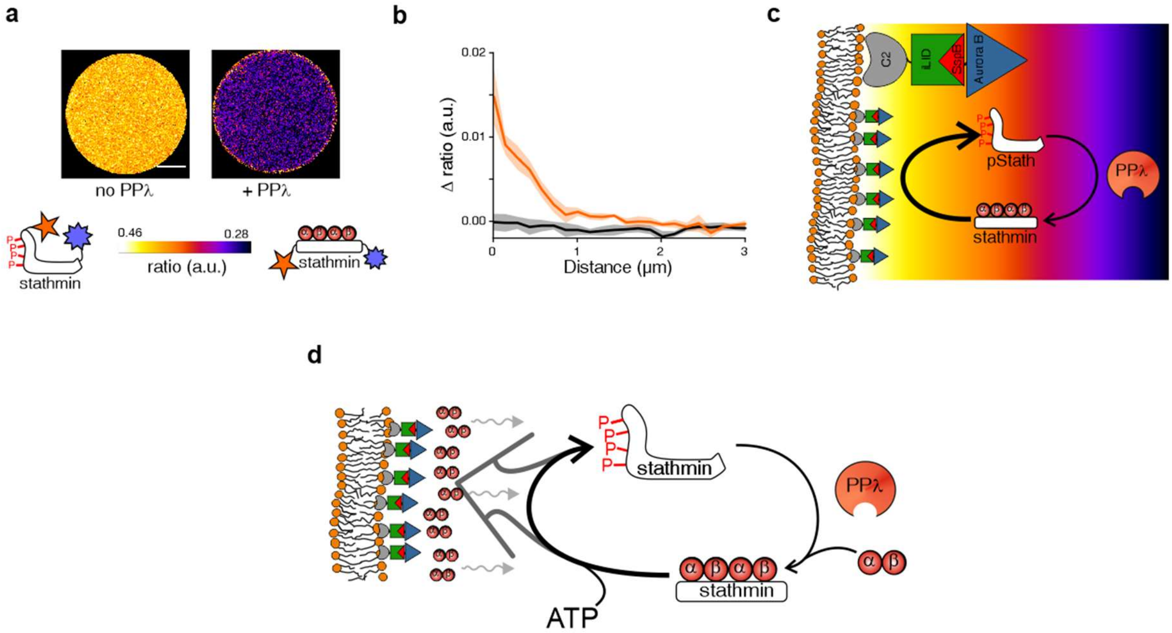

Figure 3.8: Stathmin phosphorylation gradient

(a) Ratiometric images of conformational stathmin phosphorylation FRET sensor inside GUVs upon membrane translocation of SspB-AuroraB[16]. Maximum intensity projections of 8-slice ratiometric z-stacks without (left) and with PPλ (right). (b) Corresponding ratiometric, baseline subtracted profiles of COPY° fluorescence (Δratio) inside GUVs. Without PPλ (black): mean ± S.E.M. of 6 GUVs, with PPλ (orange): mean ± S.E.M. of 4 GUVs. (c) Scheme of a phospho-stathmin gradient emanating from the membrane. Translocated SspB-AuroraB (red-blue triangles) on the membrane phosphorylates the stathmin with higher activity at the membrane (left curved arrow). Diffusing pStathmin is dephosphorylated in the cytoplasm due to the higher activity of PPλ (right curved arrow). (g) Stathmin phosphorylation cycle maintains an enhanced tubulin concentration near the membrane by SspB-AuroraB (red-blue triangles) mediated release of tubulin (red circles) from phosphorylated stathmin (dark gray arrow towards membrane), which is countered by tubulin diffusion (wavy arrows). Diffusing phosphorylated stathmin is dephosphorylated by luminal PPλ, to rebind tubulin hetero-dimers, closing the ATP driven tubulin deposition cycle. Scale bars 10 µm. Analysis and experiments were performed by K. Gavriljuk. Diagram in (d) by M. Schmick.

3.4 Dynamical features of Synthetic Morphogenic Proto-Cells

3.4.1 The reconstituted signaling system actuates the MT-aster system in GUVs with a rigid membrane

We next co-encapsulated the signaling subsystem together with the MT-aster subsystem in GUVs with a rigid membrane (isosmotic) to decide whether the light induced tubulin gradient can affect MT behavior. The concentrations of tubulin and stathmin were chosen such that the size of the aster would match the size of the GUV (45 µM tubulin, 4 µM stathmin). Indeed, upon photoactivation with blue light, we observed strong centrosome decentering and MT-growth similar to the previously observed temperature-induced-MT-growth in rigid GUVs (Figure 3.9a,b). Upon removal of the photoactivation light, the centrosome reverted to a more central position, demonstrating that MT-growth can be reversibly activated by the signaling system. This behavior was not observed in the absence of stathmin, where quantification of the Relative Centrosome Displacement (see 2.1.8) showed that the mobility of the centrosome remained equal before and after illumination with blue light (Figure 3.9c). These results show that activation of the signaling system is capable of generating MT-growth via the induced tubulin enrichment at the membrane, and that stathmin is essential to couple the light-induced signaling system to the MT-aster system.

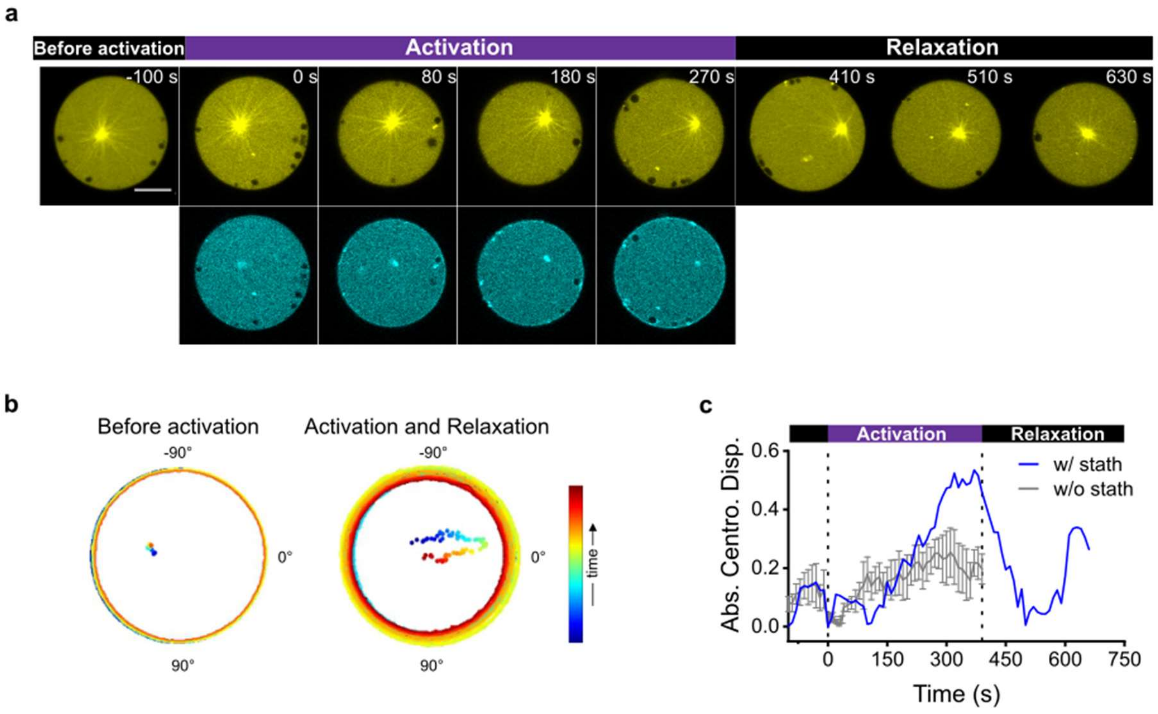

Figure 3.9: Light-induced activation of synthetic signaling leads to MT-growth

(a) Time lapse of Alexa647-tubulin (yellow, top) and Alexa488-SspB-AuroraB (cyan, bottom) in a GUV with encapsulated MT-aster/signaling system and a rigid membrane. Representative images shown for before, during, and after global illumination with blue light. (b) Corresponding GUV contours for the complete time-lapse, color coded by time progression during each phase (dots: centrosome positions). (c) Relative Centrosome Displacement for the centrosome position (Mean +/- SE) before, during and after photoactivation with blue light in the presence (blue, N=1) or absence (gray, N=4) of stathmin. Scale bar 10 µm. SynMMS were prepared and experiments were performed by K. Gavriljuk and F. Ghasemalizadeh. Analysis by B. Scocozza.

3.4.2 Enhancement of microtubule visibility

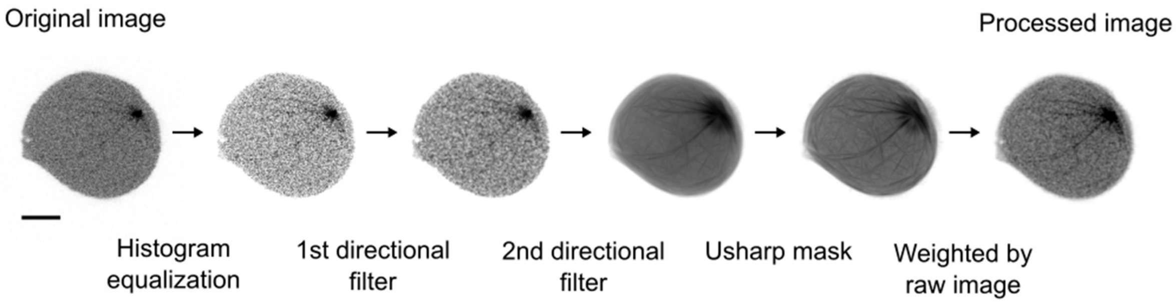

Figure 3.10: Image processing algorithm for enhancement of MT visibility

Images at the different stages of the algorithm are shown. Scale bar 10 μm.

The visibility of MTs in the Tubulin^{647} images was limited by the high background signal from free tubulin. Therefore, we set out to develop an image processing algorithm capable of enhancing MT visibility to better understand how MT-dynamics underlies morphological transitions. We found that a combination of histogram equalization, unsharp masking, and directional filtering greatly improved the visibility of MTs (see 2.1.7 for all relevant parameters). As shown in Figure 3.10, the raw image is first histogram equalized to obtain a first contrast enhancement, causing areas with low contrast to gain contrast. However, for the dimmest MTs bundles, the signal along the MT alternates between regions where the MT is visible and regions where it is barely distinguishable from the background, generating a disconnected curvilinear structure. Therefore, we applied two consecutive directional filters which enhance the contrast of thin curvilinear structures and generate connected elements. For this, a line is used as the structuring element of a mean filter, which is applied at various orientations of the line. The first directional filter uses a short line size, aimed at connecting those disconnected regions and the second directional filter uses a large line size to enhance longer interconnected curvilinear structures. This operation greatly enhances the contrast of MT bundles, but also generates spurious linear structures that need to be later suppressed. Since after directional filtering MTs can be interpreted as edges, we next apply and unsharp mask algorithm which amplifies the high-frequency components of the image, thus sharpening the contrast of edge structures. Lastly we weight the pixel values of the processed image by the values of the raw image to suppress spurious linear structures which are not present in the original image. Careful comparison of the raw and the process image in Figure 3.10 demonstrates that MT visibility is greatly enhanced. In particular, structures that cannot be observed at a first glance on the original image, can be back traced from observation of the processed image. This algorithm will enable us to better identify the connections between astral MTs and the protrusions and therefore classify the GUVs according to their morphological state, as well as to better assess the dynamics of the aster as a whole, especially in cases were MT visibility is close to noise levels.

3.4.3 Characterization of initial states for co-encapsulated signaling and MT-aster modules in GUVs with a deformable membrane

Activation of the signaling system in the rigid membrane condition allowed us to establish signaling induced MT-growth. However, these conditions do not allow for membrane deformation. We therefore decided to co-encapsulate the signaling and MT-aster systems in GUVs with a deformable membrane. This configuration will further be referred to as a Synthetic Morphogenic Membrane System (SynMMS).

We first investigated the phenotypic variability of SynMMS. Visual inspection of the global GUV morphology suggested three stable morphologies: spherical, polar and star-like. The star-like morphology was defined by a centrally positioned centrosome and multiple isotropically distributed protrusions. We found that in contrast to the encapsulated MT-aster alone, a substantial fraction of the population exhibited a star-like morphology (Figure 3.11a). To better characterize the phenotypic variability, we decided to perform a 3-dimensional morphometric analysis on the obtained shapes (Figure 3.11b, see Methods 2.1.4). Many possible morphometric measures can be considered, including moments of inertia, invariant 3D moments, solidity, extent, etc. Out of these, we found that two parameters were sufficient to separate the morphologies in different regions of the morphometric space. On the one hand, the position of the centrosome relative to the GUV, ranging from centered (0) to peripheral (1), allows to separate the polar morphologies from spherical or star-like morphologies (see 2.1.4). Namely, in the cortical and polar protrusion morphologies the centrosome has been displaced to the periphery, while the star-like exhibit a more centrally positioned centrosome. On the other hand, the “irregular parameter” is defined as the diameter ratio between the minimal bouding sphere (D), and the maximal inscribed sphere (d). This magnitude takes values close to one for ellipsoidal objects, while the presence of protrusions increases its value above one.

We then utilized these metrics to compare the phenotypic variability between the encapsulated MT-aster system alone to that of SynMMS (Figure 3.11c). The distribution in morphometric space confirmed the results of visual inspection, where more star-like morphologies were observed for the SynMMS than for the MT-aster system alone. This result suggests that basal signaling activity, may already amplify nascent protrusions which are then stabilized by the SIC process.

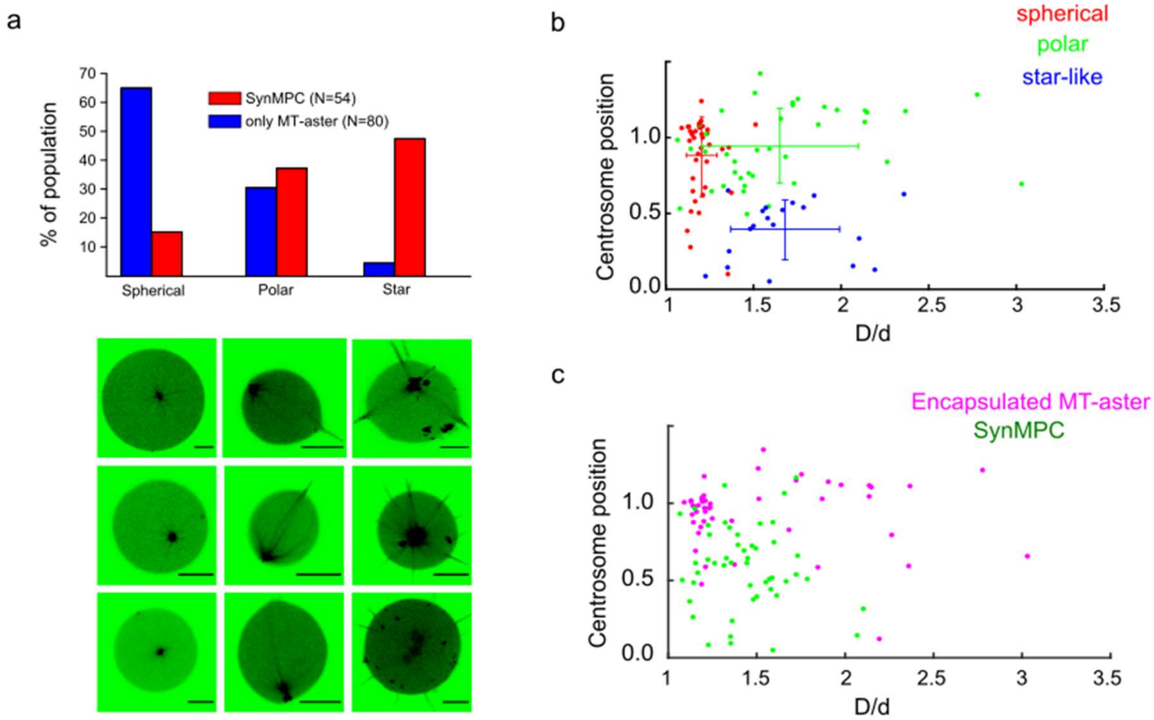

Figure 3.11: Classification of stable SynMMS morphologies

(a) Top: Distribution of morphologies for SynMMS and the encapsulated MT-aster system. Bottom: Examples of the spherical (left column), polar (middle column) and star morphologies (right column) for SynMMS. (b) Quantification in 3-Dimensions of GUV morphology by means of centrosome position and the irregular parameter D/d, (D=minimal bounding sphere, d=largest inscribed sphere) including both SynMMS and encapsulated MT-asters. Values with error bars represent the spread (mean+/-SD) of the different categories in morphometric space. (c) Same points as in (b) color-coded to show the distribution of morphologies for the encapsulated MT-aster alone (magenta) vs. SynMMS (green). SynMMS were prepared and experiments were performed by K. Gavriljuk and F. Ghasemalizadeh. Analysis by B. Scocozza.

3.4.4 Quantification of nucleation strength and relative basal translocation

To further understand the mechanisms underlying the observed SynMMS initial morphologies, we developed methods to quantify two relevant biochemical parameters. We first quantified the size of the centrosomal cluster relative to the GUV size (Relative Centrosome Surface, RCS, see Methods 2.1.6), which is indicative of the relative nucleation strength. It is fundamental to understand that generally, several centrosomes are encapsulated in one GUV which usually coalesce into one main nucleation site. The amount of centrosomes that form the final nucleation center therefore determines the nucleation strength that leads to the final

MT-density of the aster. We therefore quantified RCS as an indicator of the aster density relative to the GUV size. Quantification for the different morphologies showed that the RCS increased from spherical to polar to star, demonstrating that the nucleation strength at the centrosome, and thereby MT-density of the aster, plays a role in determining the global morphology (Figure 3.12).

On the other hand, in order to relate morphologies and their responses to the signaling activity at the membrane, we quantified the degree of SspB-AuroraB translocation to the GUV membrane, relative to the lumen signal for each time-lapse series (see 2.1.5). This also allowed to determine both, the relative level of basal signaling before activation as well as the maximal translocation obtained. Since the optical resolution was about an order of magnitude above the width of a lipid membrane, the fluorescence signal at pixels that include the membrane, contains contributions from both luminal as well as membrane localized SspB-AuroraB^{488}. To correct for the luminal contribution, the Tubulin channel was used as a reference of a luminal fluorescent signal (see 2.1.5). The obtained magnitude, R, is proportional to the fraction of SspB-AuroraB^{488} concentration at the membrane relative to the luminal SspB-AuroraB^{488}, yielding 0 in the absence of translocation and values above 0 upon translocation. This allows us to quantify the basal signaling level, R_0, as well as the fold change after activation.

It is important to note that for SynMMS, the experimental configuration did not allow for independent imaging of SspB-AuroraB^{488} without activation of signaling system. Fluorescence imaging of the Alexa488 labeled SspB-AuroraB (SspB-AuroraB^{488}) also activated the signaling system, given that the optical dimerizer iLID utilizes a LOV domain which changes conformation upon irradiation with blue light. This implies that during imaging time-lapses the state of SspB-AuroraB^{488} could not be observed before activation. Therefore, the value of basal signaling, R_0, was measured at the first frame of the activation sequence. This is a good approximation since under our experimental conditions the saturation of translocation occurred in the order of 10 frames after activation.

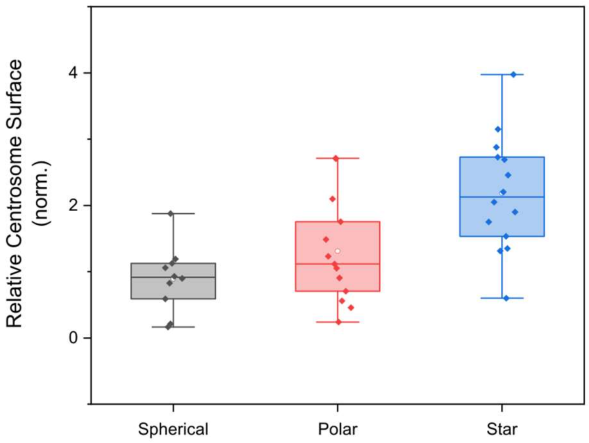

Figure 3.12: Quantification of nucleation strength for the different stable morphologies
Relative Centrosome Surface (see 2.1.6) for the spherical, polar, and star morphologies. Each point represents an individual GUV. Box delimits the 25-75 percentile interval. Line in box represents the median, white circles denote the mean.

3.4.5 Light-induced MT-growth leads to *de novo* formation of membrane protrusions

Next, we performed experiments on a SynMMS to decide if deformation could be brought by activation of the signaling system. For this, we sequentially irradiated a SynMMS with a sparsely populated MT-aster (Relative Centrosome Surface = 0.9), on localized regions and monitored the formation of protrusions. Local irradiation of the right-side led to the formation of a protrusion which persisted even after switching the irradiation off, as observed in the kymograph of local membrane curvature (Figure 3.13a-c). Subsequent irradiation on the left also led to the formation of a new protrusion which persisted after switching the activation to the lower side. This last irradiation did not lead to the formation of protrusions suggesting that MT-depletion to the other formed protrusions decreased the availability of free MTs for polymerization. In contrast, for a stimulated SynMMS lacking stathmin (SynMMS$^{\text{-stath}}$), we did not observe formation of protrusions in any of the irradiated areas (Figure 3.14), confirming that stathmin is essential for the coupling between the signaling and MT-aster systems. This results show that protrusions can be generated in SynMMSs with a small aster, which are therefore are capable of responding with directed morphological changes to local light stimulus, as if originating from localized external morphogen cues.

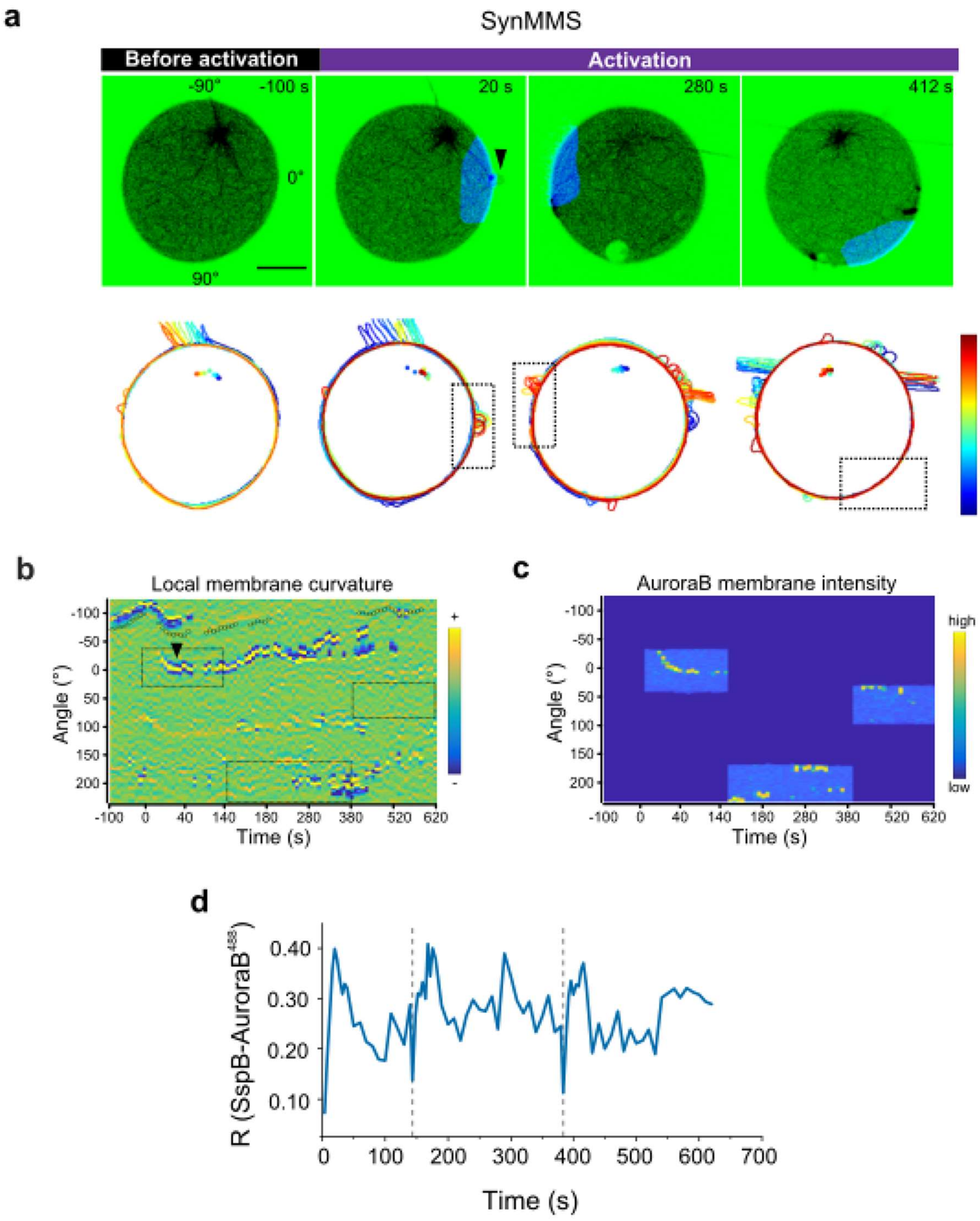

Figure 3.13: Sequential localized activation of a SynMMS with a sparsely populated MT-aster

(a) Time lapse of tubulin^{647} (inverted green, enhanced images) overlaid with translocation images of SspB-AuroraB^{488} (cyan, see 2.1.5) before and during local illumination with blue light at the equatorial plane of a SynMMS in different areas. (b) Corresponding GUV contours color coded by time progression (colored dots: corresponding centrosome positions). Black rectangles mark illumination areas. Corresponding kymographs of (c) local membrane curvature (overlaid with centrosome position, small circle: central, large circle: peripheral, black dashed rectangles denote illumination areas) and (d) SspB-AuroraB^{488} membrane intensity. Arrow heads denote protrusions of the corresponding micrographs in (a). (e) Quantified membrane translocation of SspB-AuroraB^{488}. Gray dashed lines indicate change of illumination area. Scale bars are 10µm. SynMMS were prepared and experiments were performed by K. Gavriljuk and F. Ghasemalizadeh. Analysis by B. Scocozza.

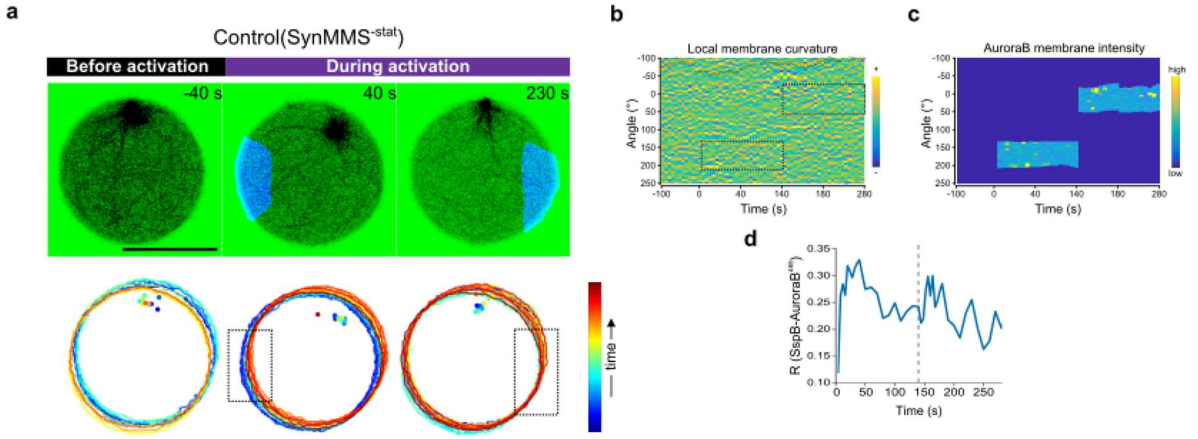

Figure 3.14: Sequential localized activation of a control SynMMS^{-stat} with a sparsely populated MT-aster

(a) Top: Time lapse of tubulin^{647} (inverted green, enhanced images) overlaid with translocation images of SspB-AuroraB^{488} (cyan, see 2.1.5) before and during local illumination with blue light at the equatorial plane of a SynMMS^{-stat} in different areas. Bottom: Corresponding GUV contours color coded by time progression (colored dots: corresponding centrosome positions). Corresponding kymographs of local membrane curvature (b, black dashed rectangles denote illumination areas) and SspB-AuroraB^{488} membrane intensity (c). (d) Quantified membrane translocation of SspB-AuroraB^{488}. Gray dashed line indicates change of illumination area. Scale bars are 10 µm. SynMMS were prepared and experiments were performed by K. Gavriljuk and F. Ghasemalizadeh. Analysis by B. Scococza.

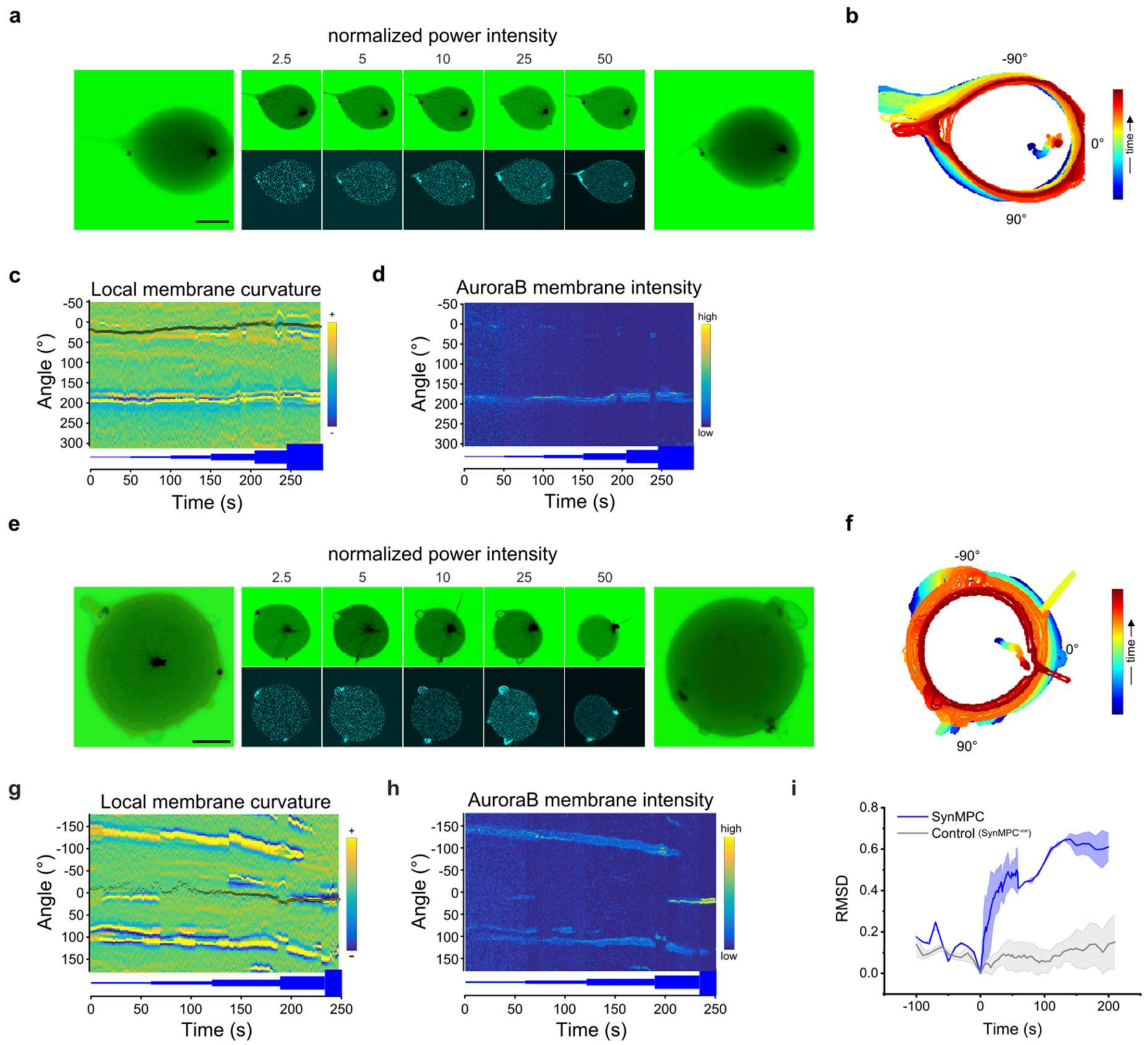

Figure 3.15: Light dose-response of SspB-AuroraB^{488} translocation on SynMMS with pre-formed protrusions

(a-d) Time lapse of tubulin^{647} (inverted green) and SspB-AuroraB^{488} (cyan) at the equatorial plane of a polar SynMMS during step-wise increase of global illumination with blue light. Maximum intensity projections of tubulin^{647} fluorescence of a confocal z-stack before (left) and after (right). Light power normalized to 1.8 mW/cm². (b) Corresponding GUV contours, color coded by time progression (colored dots: corresponding centrosome positions). Corresponding kymographs of local membrane curvature (c, overlaid with centrosome position, small circle: central, large circle: peripheral) and corresponding SspB-AuroraB^{488} membrane intensity (d), normalized to the total SspB-AuroraB^{488} intensity at each frame. (e-h) Time lapse of tubulin^{647} (inverted green) and SspB-AuroraB^{488} (cyan) at the equatorial plane of a star-like SynMMS during step-wise increase of global illumination with blue light. Maximum intensity projections of tubulin^{647} fluorescence of a confocal z-stack before (left) and after (right). Light power normalized to 1.8 mW/cm². (f) Corresponding GUV contours, color coded by time progression (colored dots: corresponding centrosome positions). Corresponding kymographs of local membrane curvature (g, overlaid with centrosome position, small circle: central, large circle: peripheral) and corresponding SspB-AuroraB^{488} membrane intensity (h). (i) Relative Centrosome Displacement of the centrosome position for SynMMSs (blue, Mean±S.E., N=4) compared to SynMMSs^{-stat} (gray, Mean ±S.E., N=4). For each light-dose an average of 3 consecutive frames is shown. Scale bars are 10µm. SynMMS were prepared and experiments were performed by K. Gavriljuk. Analysis by B. Scocozza.

3.4.6 Positive feedback between MT-aster growth and SspB-AuroraB signaling

The persistence of protrusions after removal of stimuli indicated that a feedback mechanism was responsible for their stabilization. In particular, we observed an enhanced SspB-AuroraB^{488} intensity at the newly formed protrusions (Figure 3.13c,d), suggesting that coupling between MT-induced deformations and signaling may underlie the stabilization. Therefore, we investigated if enhanced recruitment of SspB-AuroraB^{488} would also be observed in SynMMS with pre-formed protrusions. For this we performed light-dose-response experiments on SynMMSs with a polar, or star morphology, by step-wise increasing the intensity of global blue light illumination. Indeed, even at very low light doses, we observed higher SspB-AuroraB^{488} intensities at the pre-formed protrusions. In the case of the polar SynMMS, increase in the irradiation intensity coincided with a gradual broadening of the protrusion most likely due to an enhanced MT-growth at the protrusion, while no significant change in the global morphology was observed (Figure 3.15a-d). In contrast, MT-growth on the isotropically distributed protrusions of the star SynMMS, led to strong centrosome displacement (Figure 3.15e-h), which was not observed in SynMMS^{-stat} (Figure 3.15i). Importantly, MTs reorganized into a cortical MT-aster, with the protrusions either remaining in place or slightly drifting from their initial position. This contrasts the process observed in the encapsulated MT-aster system upon temperature-induced global MT growth, in which a recursive process of centrosome decentring and protrusion coalescence led to a polar morphology. The lack of coalescence in the case of SynMMS further indicates that enhanced signaling at protrusions stabilizes the SIC process by generating more efficient MT capture, which then further stabilizes the enhanced signaling in protrusions. These results show that while the MT-aster system can intrinsically stabilize protrusions through the self-induced capture mechanism, its interaction with the signaling system provides an additional layer of amplification. Thus, signaling recursively interacts with the MT-aster to further stabilize protrusions (Figure 3.16). This mechanism enables the stabilization of protrusions with lower number of MTs, which therefore do not coalesce to form a polar morphology but instead give rise to star-like morphologies.

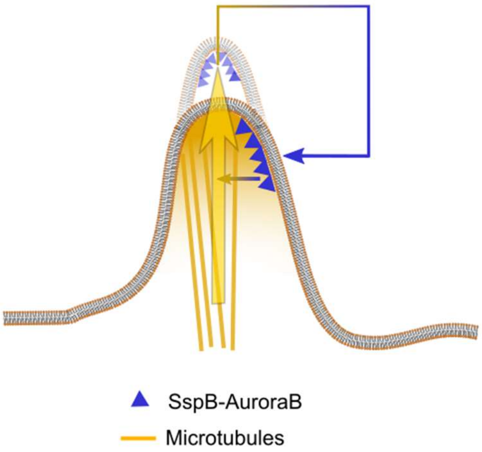

Figure 3.16: Scheme of feedback between protrusion formation and signaling activity
MT-induced deformations lead to enhanced SspB-AuroraB concentrations at the protrusion (yellow-to-blue arrow), generating higher signaling activity at protrusions. This further reinforces the deformation (yellow arrow) by inducing MT-growth (blue-to-yellow arrow), closing the feedback loop.

3.4.7 Light-induced morphological transitions depend on initial states

The previous experiments showed that global activation of a polar SynMMS did not lead to a global morphological change, suggesting that in a polar morphology, capture into the main protrusion significantly decreased the availability of free MTs for polymerization. This was concomitant with the lack of other SIC sites where growing MTs could be captured, impeding the formation of new protrusions. In contrast, global activation of a star-like SynMMS led to strong displacement of the centrosome and reorganization of the MT-aster, indicating that the response is dependent on the initial morphology.

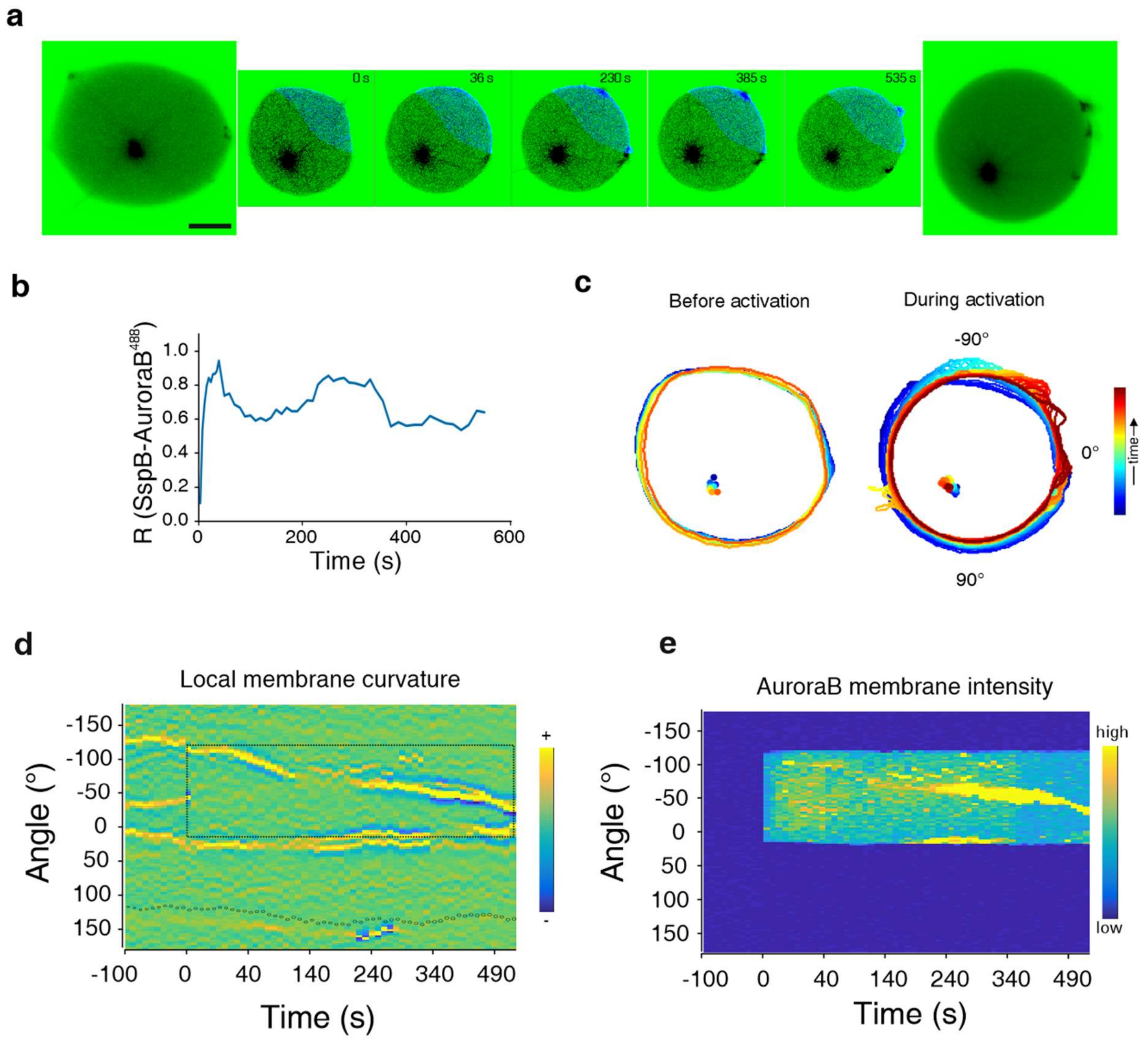

Figure 3.17: Morphological response to a localized light-signal of a SynMMS with a star morphology

(a) Time lapse of tubulin^{647} (inverted green, enhanced images) overlaid with translocation images of SspB-AuroraB^{488} (cyan, see 2.1.5) at the equatorial plane of a SynMMS with an initially star-like morphology during continuous local illumination with blue light. 3D projections of tubulin^{647} fluorescence of a confocal z-stack before (left) and after (right). (b) Corresponding quantified membrane translocation of SspB-AuroraB^{488}. (c) Corresponding GUV contours, color coded by time progression (colored dots: corresponding centrosome positions). Corresponding kymographs of local membrane curvature (d, overlaid with centrosome position, small circle: central, large circle: peripheral, black dashed rectangle denotes local illumination area) and kymograph of SspB-AuroraB^{488} membrane intensity (e). Scale bars 10 µm. SynMMS was prepared and experiments were performed by K. Gavriljuk and F. Ghasemalizadeh. Analysis by B. Scocozza.

We therefore next asked whether local activation in SynMMS with pre-formed protrusions could lead to global reorganization that is dependent on the initial morphology. We first stimulated a star-like SynMMS with weak and isotropically distributed protrusions on a localized region (Figure 3.17a, Relative Centrosome Surface = 2.1 ± 0.2). This SynMMS exhibited high basal signaling, as shown by the quantification of SspB-AuroraB^{488} relative translocation (Figure 3.17b), consistent with the stabilization of multiple small protrusions. Before activation, the morphology remained stable, as demonstrated by the local curvature kymograph and the GUV contours (Figure 3.17a,c,d). During activation in the upper right zone, the pre-existing protrusions converged towards the center of the activation region, exhibiting enhanced SspB-AuroraB^{488} intensity (Figure 3.17e). Sprouting structures were generated, most likely due to the strong acceleration of MT-growth. This resulted in a morphing process that went from star-like into a polar morphology, reorientating towards the irradiated region. Thus, star-like SynMMS with weak distributed protrusions are capable of globally reorganizing their morphology in the direction of a localized stimulus.

Based on these results, we speculated that the relative strengths between SIC amplification and signaling could underlie the dependence of response on initial state. We therefore next stimulated a SynMMS with strong but distributed protrusions and weak basal signaling (Figure 3.18a,d). In contrast to the previous SynMMS with weak protrusions, this SynMMS exhibited four strong protrusions and a strong nucleation strength (Relative Centrosome Surface = 4.0 ± 0.4). During the different stimulations, we observed sliding of MTs from distant regions into the main protrusion, indicating that net MT growth results in a net gliding force towards the main protrusion. Simultaneously, we observed a clear loss of the lower three protrusions, observable from the local curvature (Figure 3.18b). This resulted in a transition from a star-like morphology towards a morphology which kept the orientation axis of the main protrusion, flanked by two wide protrusions. Thus, local stimulation of the regions flanking the main protrusion resulted in the reinforcement of a pre-existing protrusion. This indicated that the pre-existing protrusions continuously exchange MTs through a slow escape rate from the SIC stabilized deformation, which is then increased and biased by the localized stimulation. Thus, strong protrusions act as sinks of MTs, that constrain the directionality of the response.

Altogether, these results show that a localized stimulus can lead to a global morphological reorganization in SynMMS. Both the plasticity, as well as the initial morphology, are dictated by balance between the SIC strength of the MT-aster system and activity of the signaling system. In an initial morphology that is stabilized by basal signaling activity, protrusions can be stabilized with low number of captured MTs, leaving sufficient free MTs available for global reorganization towards the light cue. In contrast, in morphologies with dominant self-induced capture, protrusions themselves constrain the morphogenic plasticity by further capturing the growing MTs, resulting in a loss of directionality in the response. Thus, signaling strength at the membrane gives plasticity to morphological responses, whereas strong SIC stabilized protrusions constrain the morphological transitions.

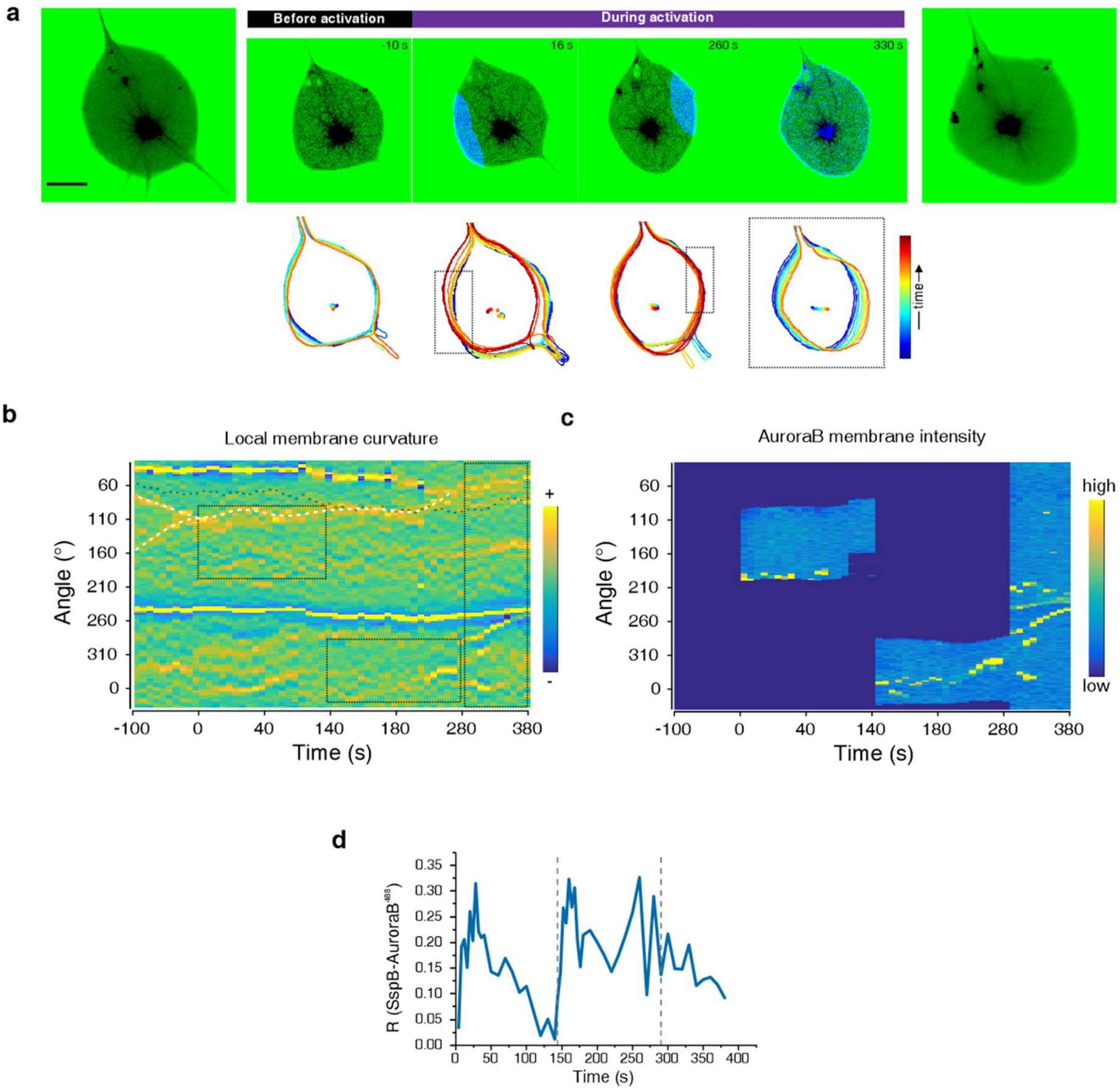

Figure 3.18: Morphological response to a localized light-signal of a SynMMS with sparsely distributed but strong protrusions

(a) Top: Time lapse of tubulin^{647} (inverted green, enhanced images) overlaid with translocation images of SspB-AuroraB^{488} (cyan, see 2.1.5) before and during local illumination with blue light of a SynMMS in different areas followed by global illumination. 3D projections of tubulin^{647} fluorescence of a confocal z-stack before (left) and after (right). Bottom: Corresponding GUV contours, color coded by time progression (colored dots: corresponding centrosome positions). (b) Corresponding kymograph of local membrane curvature (overlaid with centrosome position, small circle: central, large circle: peripheral, black dashed rectangles denote illumination areas) and (c) corresponding kymograph of SspB-AuroraB^{488} membrane intensity. (d) Corresponding quantified membrane translocation of SspB-AuroraB^{488}. Scale bars 10 µm. SynMMS were prepared and experiments were performed by K. Gavriljuk and F. Ghasemalizadeh. Analysis by B. Scocozza.

4 PART II: HYBRID CELL-COMPUTER WOUND HEALING THROUGH OPTOGENETICALLY EMULATED INTERCELLULAR COMMUNICATION

All data presented in this chapter was acquired and analyzed by the author.

4.1 Rationale

Here we develop a hybrid cell-computer experimental interface as a novel method to investigate collective behaviour arising from the communication of cells. In this setup, living cells interact with each other through a combination of virtual communication and optogenetic stimulation. The state of each cell is measured in real time, from which *in silico* cell-to-cell communication is computed and translated into optogenetic actuation that emulates emitted signaling cues. The interaction architecture can be set by the user and takes the form of a simulation. Light inputs are calculated from both the real state of the cells as well as the collective virtual state of the cell ensemble. Therefore, this setup establishes a hybrid dynamical system arising from a closed-loop between *in vitro* behavior and *in silico* communication among cells. We propose this method as a novel way to both interrogate and manipulate systems where collective behaviour emerges from the coupling of individual cells, embedded with signal processing networks.

We exemplify this approach in the context of tissue repair by creating hybrid wound healing assays (Figure 4.1). In these experiments, mammalian cells are recruited towards a virtual injury site through a virtual primary chemoattractant emanating from the wound. This primary signal induces "secretion" of a secondary virtual signal emanating from each cell which generates a field of virtual paracrine signaling. The virtual signals are then translated into optogenetic induced migration which emulates the presence of chemoattractants.

In order to create the hybrid assays, we first establish a platform for directing migration of mouse embryonic fibroblasts (MEFs) via photoactivatable Rac1 (PA-Rac1). We next develop a model of focal damage wound healing to explore the dependence of recruitment on interaction parameters. The model is based on the work done on mouse models of inducible sterile skin injury, where localized tissue damage leads to cell recruitment towards the wound site. We model migration as a Persistent Biased Random Walk (PBRW) which we adjust to the behaviour of our cells. Guided by previous studies we expand it to account for paracrine and autocrine signaling. Finally, we merge the simulations with the cell migration platform to create hybrid wound healing assays by replacing simulated cells with optogenetically actuated living cells.

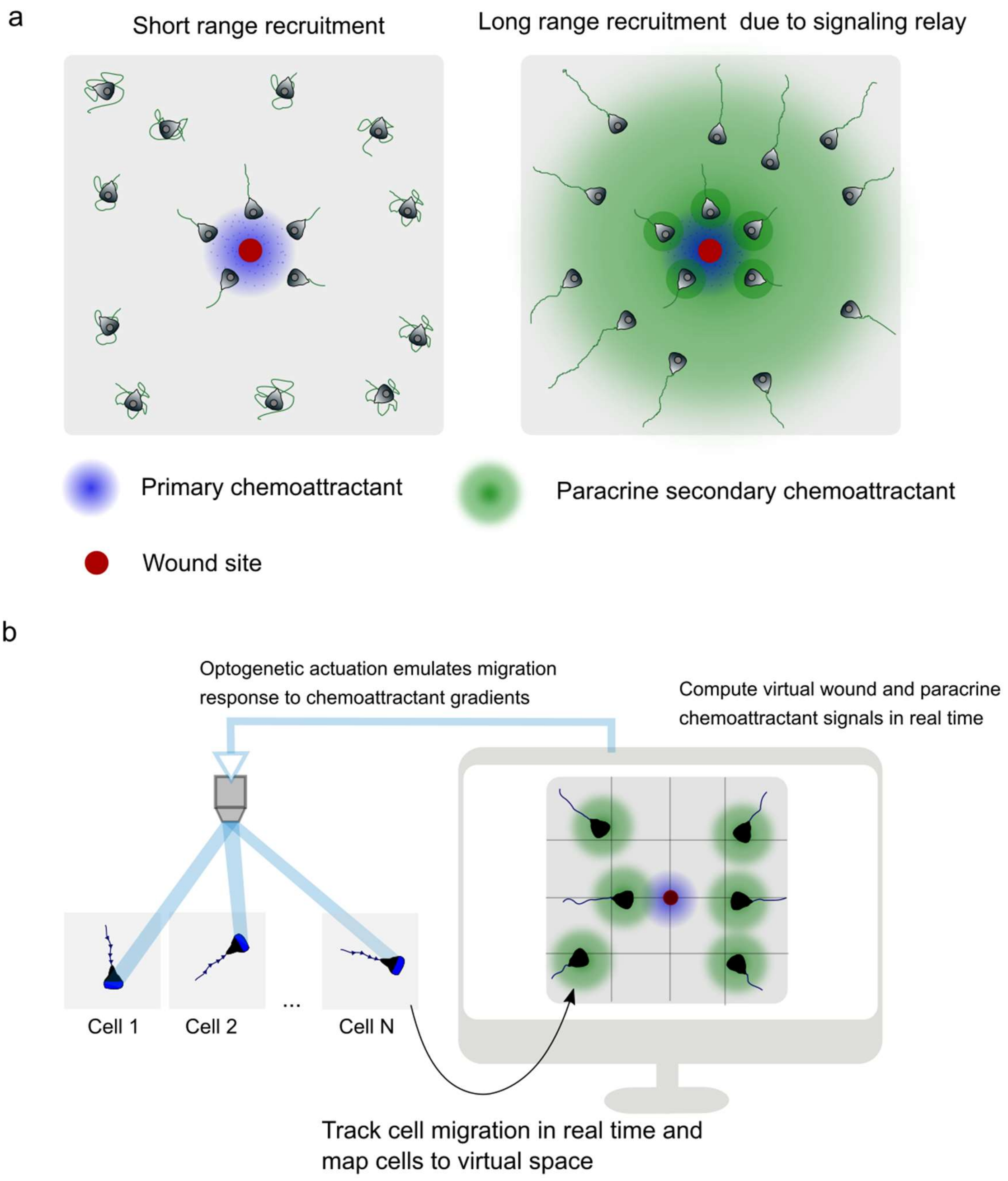

Figure 4.1: Hybrid wound healing experiments through virtual intercellular communication

(a) Scheme of cell migration towards an injury site. A primary chemoattractant signal leads to local recruitment of cells in the vicinity of the wound (left), which induces paracrine and autocrine signaling of individual cells. This relays the primary signal to distant sites, resulting in recruitment of more cells (right). (b) Scheme of experimental setup. Cells imaged at different positions are tracked in real-time and mapped into a virtual space. Virtual primary and secondary chemoattractant signals are computed in real-time during the experiment, according to the positions in virtual space. The virtual chemoattractant signals are then translated into optogenetic induced migration which emulates the presence of chemoattractants.

4.2 An automated platform for long range migration control of MEF cells

In order to mimic the response to a chemoattractant gradient, we first designed and implemented an automated workflow to direct cell migration through photoactivation of PA-Rac1. Cells expressing PA-Rac1-mCherry were imaged and tracked frame by frame, in real time. In order to produce directional migration, cells are locally photo-stimulated at the cell front, in the direction of a selected target (Figure 4.2a). Blue-light pulses with constant intensity are delivered every 1 minute to the cell front where localized irradiation is achieved through a Digital Micromirror Device (see methods 2.2.5). Results show that the automated platform could direct cellular migration for the course of 5 hours, maintaining good alignment with the target direction (Figure 4.2b). This was quantified by the chemotactic index, which measures the degree of alignment with the target direction (see Methods 2.2.6). Stimulated cells had values close to 1 indicating good alignment, while non-stimulated cells meandered around their initial position, exhibiting fluctuating values around zero (Figure 4.2c).

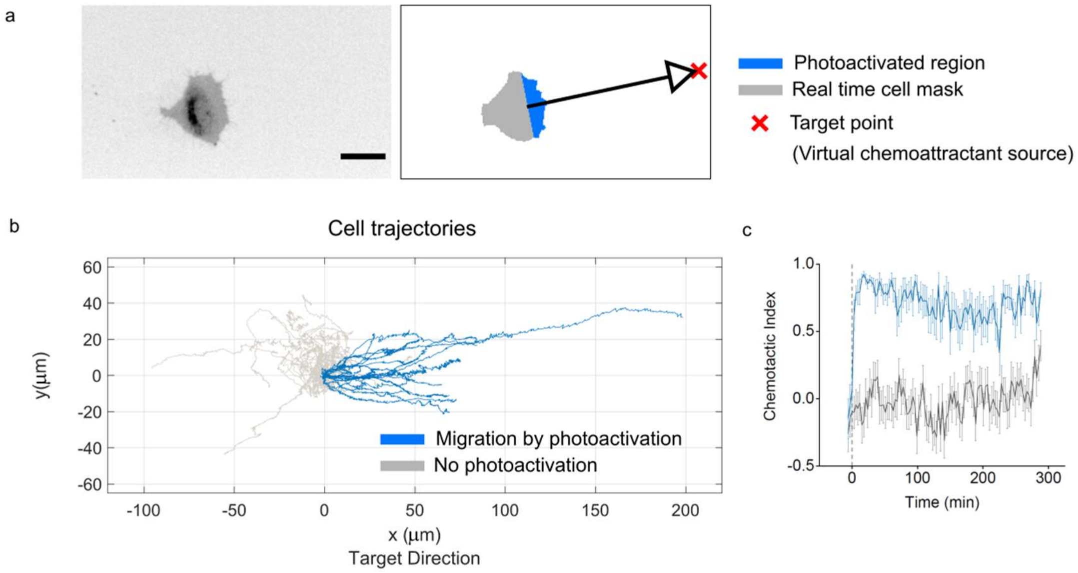

Figure 4.2: Automated platform for directing migration via PA-Rac1 photoactivation
(a) Left: micrograph of cell expressing PA-Rac1-mCherry during optogenetic induced migration. Right: corresponding real time cell mask and photo activated region in the direction of the target

point, which mimics a virtual source of chemoattractant. (b) Cell tracks upon optogenetic induced migration (blue, duration = 5 hours, N = 17) or in the absence of photoactivation (gray, duration = 5 hours, N = 27). Cell tracks start at the origin and are targeted to the positive x direction. (c) Corresponding time series of the chemotactic index (Mean±SE). Negative time: before activation.

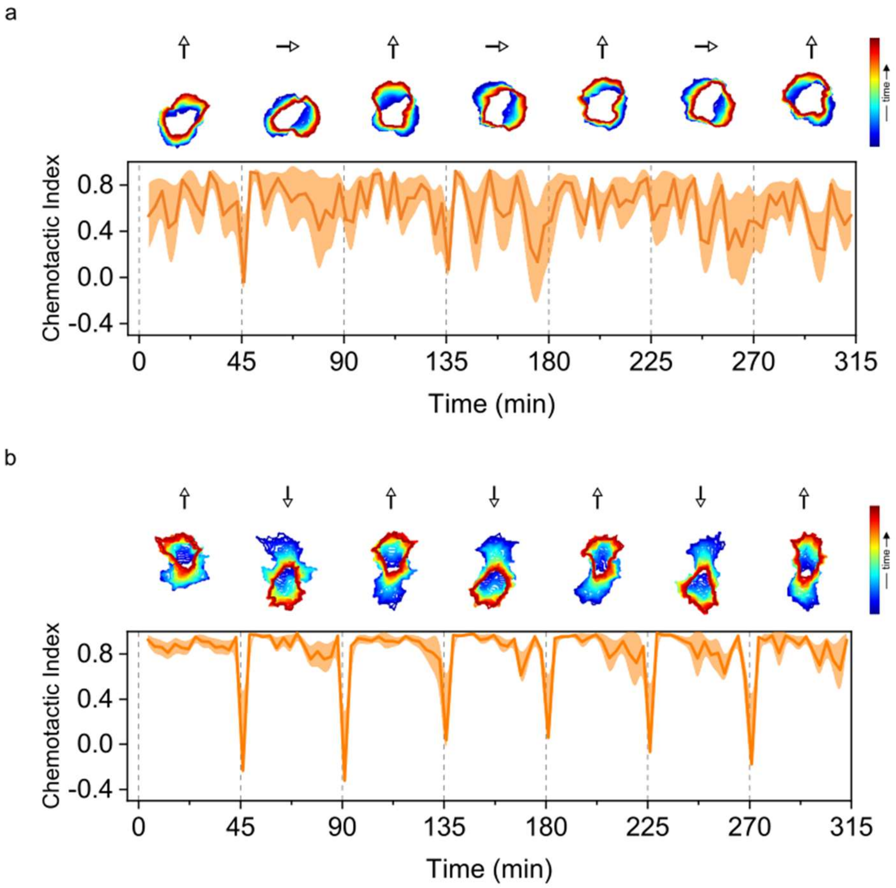

Figure 4.3: Reorientation of migration directionality through PA-Rac1 photoactivation
(a) Top: contours of cell shape color-coded by time progression for each phase of the time-lapse, as the target point was rotated by 90 degrees. Arrows on top indicate direction in which the cells were photoactivated. Bottom: quantification of chemotactic index, Mean±SE, N = 7. (b) Quantification as in (b) for a rotation of 180 degrees of the target point. N = 8.

However, in physiological environments, cells do not perceive fixed chemotactic cues, but rather spatiotemporally varying chemoattractant gradients. Therefore, we targeted cells to a specific point and then induced either a right angle rotation or a complete reversal of the target point. Upon change in the photoactivation region, cells in fact turned towards the direction of the new target point, and could even completely revert its migration direction, keeping a high chemotactic index (Figure 4.3). Altogether, these results show that the proposed migration control method by light activation, is capable of directing cell migration, mimicking the exposure to a changing chemoattractant gradient.

4.3 Simulations of collective behavior during cell recruitment towards an injury site

In order to establish the interaction relationships and parameters for the hybrid assay, we next set out to model and simulate cell recruitment towards an injury site. The model was guided by previously reported observations in focal damage wound healing experiments[27], where a short two-photon laser pulse induces tissue damage, leading to neutrophil swarming towards the injury site.

We first modeled cellular motility as a Persistent Biased Random Walk (PBRW), which has been shown to be a good approximation of motile behavior in different cell types[52,55–57]. Since the PBRW corresponds to the mean reverting Ornstein-Uhlenbeck process, the influence of chemoattractants on motility can be introduced as a bias term that generates a drift in the random walk. This is described by the equation:

$$\frac{\mathrm{d}\mathbf{v}}{\mathrm{dt}} = -\frac{1}{\tau}\mathbf{v}(\mathrm{t}) + \frac{\sqrt{2D}}{\tau}(\mathbf{n}(\mathrm{t}) + \mathbf{u}(\mathrm{t}))$$

Eq. 1

where $\mathbf{v}$ is the velocity of the cell, τ is the persistence, D describes the diffusivity of the motion, $\mathbf{n}$ is white noise and $\mathbf{u}$ is the bias term. These parameters depend on the cell type, substrate, as well as the chemoattractant potency (real or emulated by optogenetics) and were matched to our experimental conditions (see Methods 2.2.8).

We next expanded the PBRW to model paracrine and autocrine signaling among cells through a secondary signal, whose production depends on the primary chemoattractant emanating from the injury site. In this way, we can model collective behaviour during cellular swarming, as occurring under physiological conditions[27]. We first simulated the case where cells are only affected by a primary chemoattractant emanating from the wound. The concentration of the chemoattractant is described as a gaussian decay from the focal site of injury

$$C_1(\boldsymbol{x}) = A_w exp\left(1 - \frac{\|\mathbf{x} - \mathbf{x}_w\|^2}{R_w^2}\right)$$

Eq. 2

where $C_1(\mathbf{x})$ is the concentration field of the primary chemoattractant produced at the injury site at position $\mathbf{x}$, with amplitude A_w, extent R_w and centered at $\mathbf{x}_w$. This concentration field is then translated into a motility bias $\mathbf{u}$ towards the wound. Previous experimental studies show that once cells engage directed swarming, they do so at a constant speed (Figure 1.3b)[27,29]. Therefore, we set the bias vector $\mathbf{u}$, to be a constant vector in the direction of the injury when the concentration of primary chemoattractant is above a threshold:

$$\mathbf{u}_i(t) = \begin{cases} \mathbf{0}, & C_1(\mathbf{x}_i(\mathrm{t})) < T \\ u\boldsymbol{d}_i(t), & C_1(\mathbf{x}_i(\mathrm{t})) \geq T \end{cases}$$

Eq. 3

with

$$\boldsymbol{d}_i(\mathrm{t}) = \frac{\mathbf{x}_i - \mathbf{x}(\mathrm{t})}{\|\mathbf{x}_i - \mathbf{x}(\mathrm{t})\|}$$

Eq. 4

where $\mathbf{u}_i$ is the bias vector of cell i, having strength u and directed towards the wound, $\boldsymbol{d}_i(\mathrm{t})$, when primary chemoattractant concentration is above the threshold T. This simplification also makes the simulations consistent with our experiments, in which cells are either stimulated or not stimulated, allowing us to determine u from the experiments in Figure 4.2 (see 2.2.8). The presence of this threshold thus defines supra- and sub-threshold regions in which cells engage or not in chemotaxis.

For the simulations, we arranged cells in three concentric rings to account for regions that were proximal, distant, and far away from the wound (see Methods 2.2.7 and 2.2.9). The bias threshold was set at the value separating the proximal and distant sites, so that only cells close to the wound (first ring) would be recruited. Simulations under these conditions indeed showed only cells within the first ring were recruited (Figure 4.4a). This was reflected in the distance–time plot (Figure 4.4b), which shows the distance to the wound as a function of time for each cell, color-coded by the chemotactic index. Cells in the outer regions meandered around their initial position, reflected in a chemotactic index fluctuating around 0, while recruited cells exhibited a high chemotactic index value.

Next we modeled communication among cells through paracrine signaling, which has been shown to generate a signaling relay that effectively increases the recruitment radius of the injury[27]. These secondary signals are produced in response to primary chemoattractants[29], in a concentration dependent manner. Thus, the paracrine signal emanating from cell i, $C_2^i(\boldsymbol{x},\mathrm{t})$, can be written as:

$$C_2^i(\mathbf{x},\mathrm{t}) = A_p C_1(\mathbf{x}_i(\mathrm{t}))\exp\left(-\frac{\|\mathbf{x}-\mathbf{x}_\mathrm{i}(\mathrm{t})\|^2}{R_P^2}\right)$$

Eq. 5

where $A_P$is an amplitude constant and R_P is the decay length at *1/*e of the paracrine signal. In consequence, the total paracrine field is the sum of gaussian decays from each cell:

$$C_2(\mathbf{x},\mathrm{t}) = \sum_{i\in Cells} C_2^i(\mathbf{x},\mathrm{t})$$

Eq. 6

This paracrine signal has to be translated into a bias in the motility. These secondary signals can be chemoattractants in themselves, like LTB4, that might influence the directionality of migration. However, LTB4 has also been shown to act by sensitizing cells to the primary chemoattractant fMLP, facilitating its polarization[29]. Guided by this observation, we define the bias such that the paracrine field acts by enhancing the effective perceived concentration of primary chemoattractant. The effective primary chemoattractant signal at cell *i* and time t can be then described as:

$$C_{\mathrm{eff}}^i(\mathbf{x}_\mathrm{i},\mathrm{t}) = C_1\left(\mathbf{x}_\mathrm{i}(\mathrm{t})\right) + C_2(\mathbf{x}_\mathrm{i},\mathrm{t})$$

Eq. 7

This implies that the result of intercellular communication is to effectively lower the signal threshold that leads to migration. The bias can be then written as

$$\boldsymbol{u}_i(t) = \begin{cases} \mathbf{0}, & C_{\mathrm{eff}}^{\mathrm{i}}(\mathbf{x}_\mathrm{i},\mathrm{t}) < T \\ u\boldsymbol{d}_i(t), & C_{\mathrm{eff}}^{\mathrm{i}}(\mathbf{x}_\mathrm{i},\mathrm{t}) \geq T \end{cases}$$

Eq. 8

We then performed simulations undergoing interaction via secondary signals. We observed that not only cells within the proximal region were recruited, but also cells from distant sites were recruited (Figure 4.4d-e). As cells migrated towards the wound, the supra-threshold region was enlarged, leading to a larger recruitment radius (Figure 4.4f). As cells approach the wound, they perceive a higher concentration of primary signal, which in turn increases their paracrine signal secretion. This gradual increase in the strength of the secondary field, steadily increases the perceived primary signal in cells from distant sites until it crosses the threshold, thereby engaging stable chemotaxis at later time points. This delay depended on the strength of the paracrine signaling amplitude A_p, as demonstrated by the time evolution of the average recruitment radius under different conditions (Figure 4.5a). Simulations also showed that final average recruitment radius had a stronger dependence on the extent of paracrine signaling R_P than on the amplitude, A_p (Figure 4.5b). In particular, as the extent of the paracrine signal approaches half the separation between regions, a 1.5-fold enhancement in the recruitment radius is observed across different amplitudes. Taken together, these results show that our model can recapitulate coordinated cellular migration towards an injury site, arising from the intercellular communication triggered by a wound.

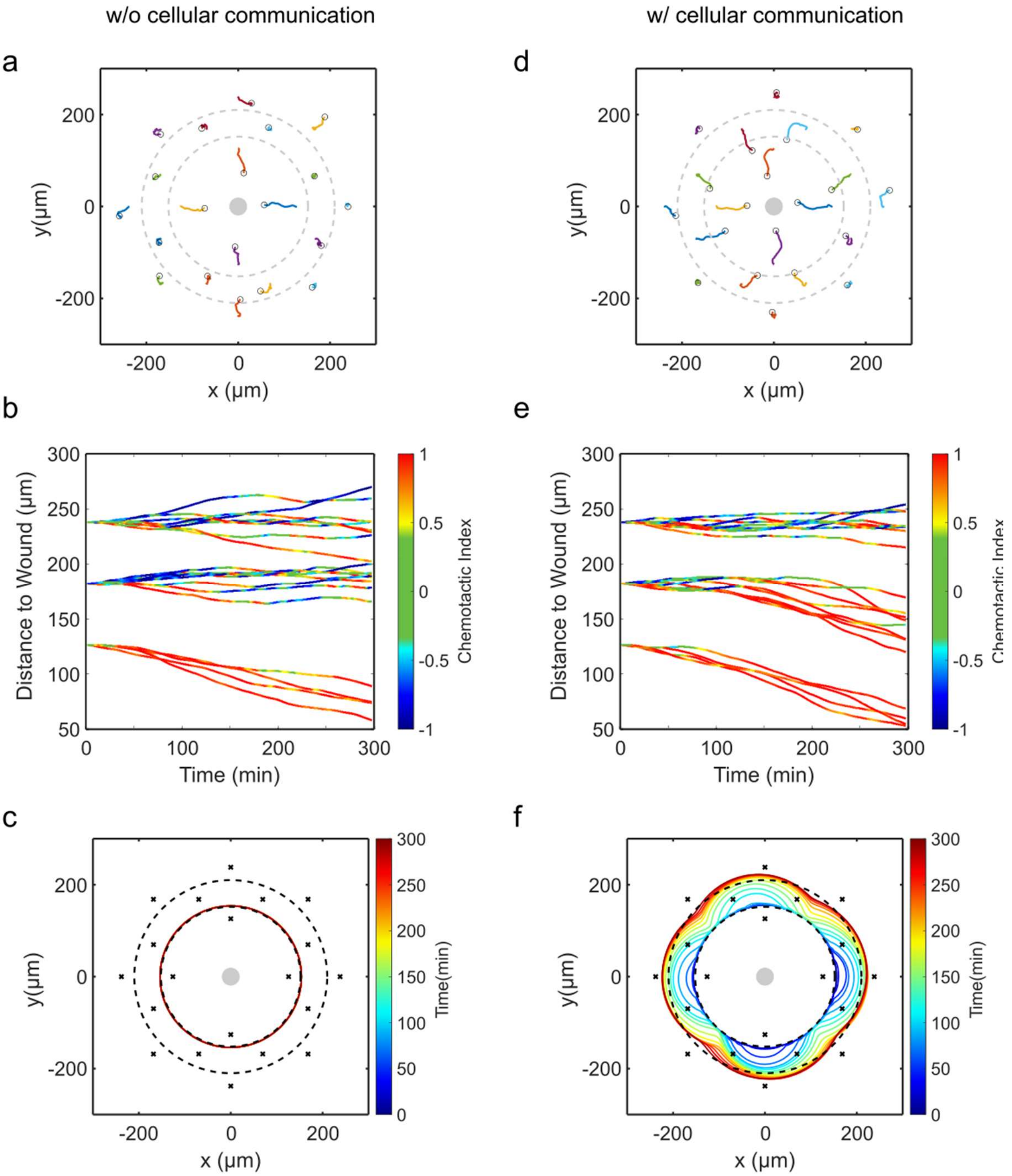

Figure 4.4: Simulations of cell recruitment towards an injury site

(a) Simulated cell traces of migration in the presence of an injury site (denoted by grey circle) emitting a gradient of primary chemoattractant (Eq. 2) and in the absence of paracrine signaling. Black circle indicates the position at the end of the trace. Dashed circles separate proximal, distant and far regions. (b) Corresponding distance to the wound as a function of time. Traces are color-coded according to their chemotactic index. (c) Evolution of the recruitment region (supra-threshold region) color-coded by time progression. (d-f) as in (a-c) but in the presence of paracrine signaling (A_p=10^{-9}).

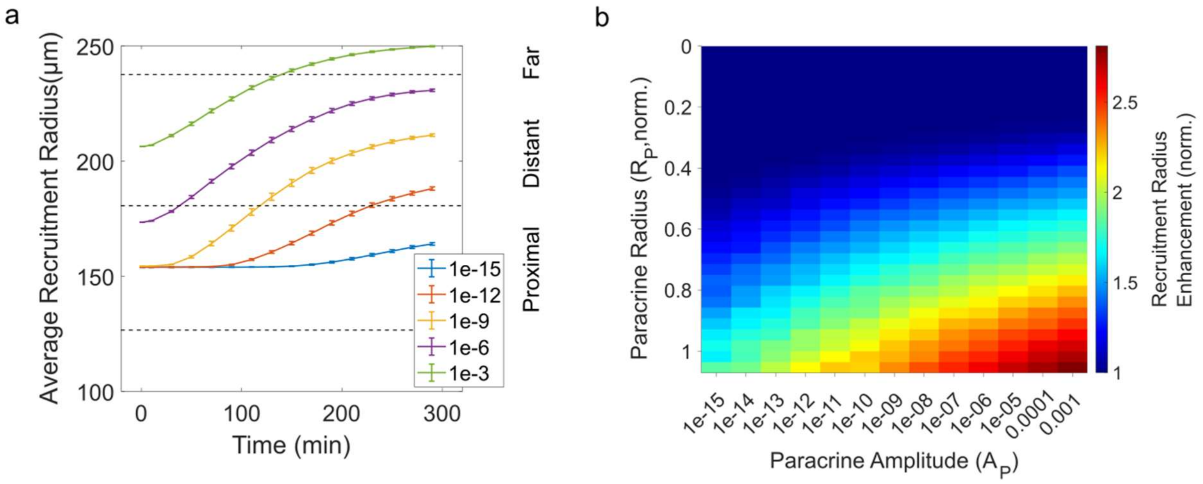

Figure 4.5: Recruitment radius dependence on paracrine signaling amplitude and extent (a) Evolution of average recruitment radius as a function of the paracrine amplitude A_P (Mean ±SE, N=25). Grey dashed lines separate the proximal, distant and far regions. (b) Enhancement in the average recruitment radius at the end of the simulation (t=300 min) for different paracrine amplitudes and extents (N=5 for each pixel). Enhancement normalized to recruitment radius in the absence of paracrine signaling. Paracrine Radius normalized to the distance between the regions (twice the average cell size = 56 μm, see 2.2.7).

4.4 Virtual intercellular signaling generates a hybrid wound healing assay that recapitulates features of *in vivo* wound healing

Finally, we set out to perform hybrid experiments where living cells receive photoactivation signals from a simulated focal tissue damage. Cells respond to a virtual chemoattractant signal from the injury site as well as to from virtual paracrine and autocrine signaling. For this, we first mapped cells into a virtual space arranging them into three concentric rings (see Methods 2.2.9), as for the simulations. The migration control platform was then integrated with the simulations by replacing the simulated random walk with mapped positions of living cells. At each iteration, cells are imaged, and their position in virtual space is calculated. From this, primary and secondary paracrine virtual signals are calculated according to the model. Cells are then photo-stimulated towards the wound if the effective primary signal is above threshold. In this manner, the behaviour of the cells is not predetermined but evolves according to a closed-loop between cellular responses and virtual communication, without user intervention.

We therefore set out to run hybrid experiments, for which we mapped the cells to virtual cells as for the simulations, keeping all parameters the same. We observed that in the presence of the virtual primary signal alone, only the cells in the first ring region were recruited, with no expansion of the supra-threshold region (Figure 4.6a-c). Cells in the outer regions wandered around their starting position with a chemotactic index fluctuating around zero. Instead, when the virtual paracrine signaling was present, cells from distant sites could also be recruited, as a direct consequence from the enhancement of the recruitment region (Figure 4.6d-f). Distant cells engaged delayed directed migration as predicted by the model.

Altogether, these results consolidate a proof of concept for the implementation of cell-computer interfaces, in which hybrid *in silico*-*in vitro* experiments phenocopy feature of *in vivo* wound healing.

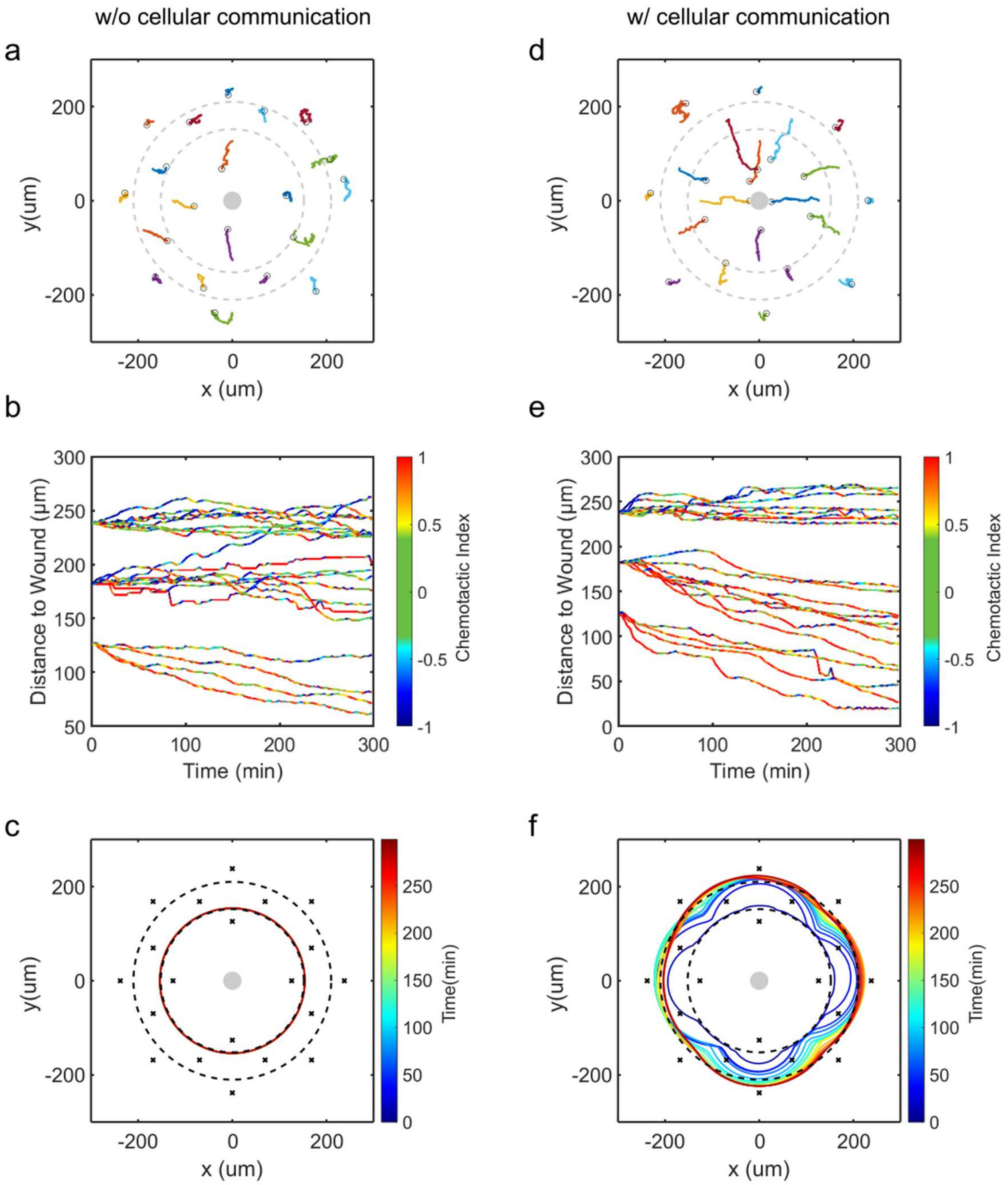

Figure 4.6: Live cell experiments of hybrid wound healing with virtual light communication

(a) Living cell migration traces in the presence of a virtual injury site (denoted by grey circle) with a gradient of virtual primary chemoattractant, in the absence of emulated paracrine signaling. Black circle indicates cell position at the end of the trace. Dashed circles separate proximal, distant and far regions. (b) Corresponding distance to the wound vs. time for the experimentally obtained traces. Traces are color-coded according to their chemotactic index. (c) Evolution of the recruitment region (supra-threshold region) color-coded by time progression. (d-f) as in (a-c) but in the presence of virtual paracrine signaling.

5 DISCUSSION

5.1 Part I: A synthetic morphogenic membrane system that responds with self-organized shape changes to local light cues

To elucidate fundamental principles of cell morphogenesis, we investigated the dynamics that emerged from the collective behaviour of MT-asters and a reconstituted signaling system encapsulated in liposomes. Investigation of the MT-aster sub-system dynamics in the absence of signaling, already showed that the activity of single MTs is coordinated through an indirect interaction mediated by the deformable membrane. We demonstrated that MT-aster system exhibited self-organized morphogenesis, based on amplification of MT-induced protrusions, which at the same time depletes free MTs, leading to stabilization of shape. This process is analogous to Grassé's concept of stigmergy describing the collective behaviour of social insects, which through indirect communication can create self-organized nest structures[58].

Introducing the signaling subsystem allowed modulation of the intrinsic dynamics of the MT-aster system by transduction of light signals into gradients of stathmin activity. Analogously to the stathmin-kinase translocation to the membrane in the Rac1-PAK1 network, a local light signal recruits SspB-AuroraB from the cytosol to membrane associated C2-iLID. This results in a dimensionality reduction from 3D (lumen) to 2D (GUV membrane) increasing kinase activity for its cytosolic substrate stathmin. In this way, the dephosphorylating activity of the cytosolic phosphatase PPλ can be overridden. This shifts the phosphorylation-dephosphorylation cycle towards phosphorylated stathmin in the membrane proximal cytosol, which together with stathmin diffusion lead to a steady-state phospho-stathmin gradient. This phospho-stathmin gradient thereby promotes directional MT-growth towards the stimulated membrane region.

Development of morphodynamic analysis tools, such as local curvature kymographs allowed us to follow protrusion dynamics and its relation to signaling at the membrane. Crucially, we found that the coupling between signal transduction and MT-dynamics is indeed bi-directional. Not only signaling affects MT-growth, but MT-induced deformation concentrates SspB-AuroraB in protrusions, enhancing signaling, resulting in a positive feedback interaction. We further demonstrated that the deformable membrane is key in mediating this positive feedback mechanism, showing that amplification occurs without any direct molecular feedback, but rather, due to geometric features that locally affect biochemical reactions. This means that the system as a whole cannot be understood by linear causality descriptions, but rather, that the recursive interaction between MT-aster dynamics and signaling dynamics at the deformable membrane determines both the initial morphological states as well as the response of the whole system.

Our observations show that signaling strength at the membrane provides plasticity in the morphogenic response, while strong MT-aster activity leads to stabilization of shape. This balance between plasticity and robustness is dictated by the amount, strength and distribution of protrusions. In the presence of multiple but small protrusions, the system has multiple directionalities available for engaging amplification upon a local stimulus. Such local stimuli enhance the exchange of MTs between protrusions thereby locally amplifying a preexisting protrusion. In contrast, when few but strong protrusions are present, they constrain the directionality of the response by acting as strong sinks of the growing MTs.

Although living cells employ many mechanisms to regulate their morphological identity, our results hint on how the plasticity and stabilization could be achieved. One could further ask how external stimuli guide cells into one or the other mode. The interaction of the MT and actin networks might underlie this transition: while actin networks operate at faster timescales and at the periphery of cells, the globally coordinated MT-aster determines the global shape. Such questions could be further investigated in reconstituted systems that include both actin and MT networks, taking advantage of recent advances in reconstitution of actin networks[59]. In addition, motor proteins that interact with MTs could be introduced to investigate other layers of regulation that affect the self-organization of MT-asters.

The life span of SynMMS is limited by availability encapsulated ATP and GTP. This could be extended by incorporating artificial photosynthetic systems[60,61] which convert light energy into ATP or GTP, keeping the synthetic cells out-of-equilibrium. Recent advances in reconstitution of bacterial cell division and self-replicating DNA by its own encoded proteins in liposomes, could enable self-replication of reconstituted proto-cells.

At the higher scale, progress has been made in the generation of synthetic tissues where porous proto-cells communicate by diffusive protein signals to form larger tissue-mimicking arrays[50]. The intrinsic self-organizing morphological dynamics of SynMMS will allow to establish recursive intercellular communication[7], enabling to uncover how the intrinsic morphological dynamics of individual entities can be coupled by intercellular communication to investigate higher scale functions such as tissue formation and repair.

5.2 Part II: Hybrid cell-computer wound healing through optogenetically emulated intercellular communication

To investigate the dynamics that emerges from the coupled behaviour of communicating cells, we conceptualized and created a hybrid cell-computer interface. This interface enables the execution of hybrid experiments in which a part of the events occurs *in silico* and a part *in vitro*, where living cells affect each other through *in silico* communication. We demonstrated that optogenetic closed-loops can be used not only for cellular control of molecular actuators, but will also help elucidate how collective behaviour arises from intercellular communication.

The developed automated platform for migration control could direct mouse embryonic fibroblasts (MEFs) via photoactivatable Rac1 (PA-Rac1). This platform could be applied almost directly to any other form of optical actuation of the cytoskeleton, by adapting the stimulation protocol for the desired cellular behaviour or cell type. For example, shape changes could be induced through other optogenetic tools, such as optical dimerizers that translocate GEFs to the plasma membrane, to investigate the role of different effectors in coordinating cellular behaviour. Interestingly, emulated communication by actuation of more downstream molecules would only couple a sub set of the transduction network which could help uncover their differential role. In addition, in the last years, photoswitchable small molecules were developed based on small molecule inhibitors of cytoskeletal activity[62], which could be implemented as actuators that directly regulate dynamical features of the cytoskeleton, such as stabilization or de-stabilization of microtubules. This would enable assessment of how higher order features, rather than molecular players, are implicated in cellular communication. The later aligns strongly with the philosophy of our approach, which is intended to find more abstract dynamical features in collective behaviour, rather than identification of molecular players.

On the other hand, we developed a model of a focal damage wound healing incorporating physiological mechanisms identified in previous experimental studies. We showed that if paracrine and autocrine signaling act by sensitizing cells to the primary chemoattractant, there is an enlargement in the recruitment radius, consistent with previous studies. The model was used to explore the influence of interaction parameters on the enlargement and thereby pre-establish the conditions for the hybrid assays. This enabled us to successfully merge the simulations with the cell migration platform to create hybrid wound healing assays. These hybrid experiments showed that under virtual communication, cells from distant sites are recruited by a paracrine mediated expansion in the recruitment region. Thus, the behavior of the cell ensemble resulted from a mixed dynamics between *in vitro* cellular behavior and *in silico* communication among cells.

At the same time, our approach could be improved by incorporating reaction-diffusion models to account for more realistic spatio-temporal features of paracrine and autocrine signaling. In addition, the model did not include direct chemotaxis induced by the secondary chemoattractant and future experiments could be performed to assess the different features that arise when one or the other effect dominates. Future experiments could be performed by optogenetically actuating neutrophils to closely resemble physiological circumstances. Different cell types could be co-cultured, such as monocytes and neutrophils, to explore if crosstalk between them can explain experimental observations. Furthermore, advances in 3D fluorescence imaging in deep tissue[63–65] will allow to conduct such hybrid experiments in more realistic contexts such as mouse models of sterile skin injury.

A powerful feature of this approach is the flexibility to decide which aspects of the experiments will be implemented *in silico*, and which aspects are implemented in real cells. Therefore, the balance between physiological events and simulations can be adapted to the desired purpose, with more weight towards one or the other. On the one hand, this significantly improves on pure simulations by incorporating the natural behaviour of living cells, avoiding modelling assumptions of cellular behaviour. At the same time, by replacing a part of simulated behaviour with behaviour of real cells, models of cellular behaviour can be tested. On the other hand, this flexibility opens the possibility to put under control variables which are not under control in physiological environments, such as spatial arrangement of cells, signaling strengths, diffusion constants, etc. For example, while the intrinsic motility parameters of the cells can be retrieved from experimental data, other parameters such as the spatial extent of the paracrine signal, or its strength, might be hard to measure, especially in physiological contexts. Furthermore, in our experiments we actuated PA-Rac1 which directly induced motility, and read out motility. This means that the functional distance between readout and actuation was small. Instead, if an observable that is either not directly related or whose relationship to actuation is unknown, dynamical features of their relationship could be uncovered.

The approach is not limited to the understanding of underlying principles but could potentially be used as a tool to manipulate living systems in a systemic way. That is, expanding the dynamical solutions of cells by equipping them with new dynamical features, coming from the interface. This could reveal, for example, which dynamical capabilities are lacking in unhealthy cells incapable of handling external threats, and enhance them with additional information processing capabilities to fight disease.

Our results demonstrate that hybrid cell-computer interfaces constitute a novel experimental tool for systemic investigations that bridge the gap between experiments and modeling, with potential applications in manipulation of collective cellular behavior to treat disease from a systemic perspective.

5.3 Summary

In summary, investigation of the dynamical behaviour of a Synthetic Morphogenic Membrane System (SynMMS) allowed us to uncover fundamental principles of morphogenesis: how plasticity and robustness to external morphogen cues can be attained. We found that recursive interactions between the signaling and MT-aster dynamics, create self-organized morphologies and underlie reorganization in the direction of external light cues. At a higher scale, the coupling of cellular processing networks leads to functional collective behaviour during wound healing. Our novel hybrid real-cell / virtual-communication experimental interface enables control of parameters which are hard to measure or regulate under physiological conditions. In the future, interaction of synthetic and living systems will enlighten further understanding of living matter.

6 REFERENCES

1. Bonabeau, E., Theraulaz, G., Deneubourg, J. L., Aron, S. & Camazine, S. Self-organization in social insects. *Trends in Ecology and Evolution* vol. 12 188–193 (1997).
2. King, H., Ocko, S. & Mahadevan, L. Termite mounds harness diurnal temperature oscillations for ventilation. *Proc. Natl. Acad. Sci. U. S. A.* **112**, 11589–11593 (2015).
3. Kearns, D. B. A field guide to bacterial swarming motility. *Nature Reviews Microbiology* vol. 8 634–644 (2010).
4. Bazazi, S. *et al.* Collective Motion and Cannibalism in Locust Migratory Bands. *Curr. Biol.* **18**, 735–739 (2008).
5. Flack, A., Nagy, M., Fiedler, W., Couzin, I. D. & Wikelski, M. From local collective behavior to global migratory patterns in white storks. *Science (80-.).* **360**, 911–914 (2018).
6. Nagy, M., Couzin, I. D., Fiedler, W., Wikelski, M. & Flack, A. Synchronization, coordination and collective sensing during thermalling flight of freely migrating white storks. *Philos. Trans. R. Soc. B Biol. Sci.* **373**, 20170011 (2018).
7. Koseska, A. & Bastiaens, P. I. H. Cell signaling as a cognitive process. **36**, 568–582 (2017).
8. Huber, F., Boire, A., López, M. P. & Koenderink, G. H. Cytoskeletal crosstalk: When three different personalities team up. *Current Opinion in Cell Biology* vol. 32 39–47 (2015).
9. Etienne-Manneville, S. Actin and microtubules in cell motility: which one is in control? *Traffic* **5**, 470–477 (2004).
10. Etienne-Manneville, S. Microtubules in Cell Migration. *Annu. Rev. Cell Dev. Biol.* **29**, 471–499 (2013).
11. Muroyama, A. & Lechler, T. Microtubule organization, dynamics and functions in differentiated cells. *Development* **144**, 3012–3021 (2017).
12. Vignaud, T., Blanchoin, L. & Théry, M. Directed cytoskeleton self-organization. *Trends Cell Biol.* **22**, 671–682 (2012).

13. Kapitein, L. C. & Hoogenraad, C. C. Building the Neuronal Microtubule Cytoskeleton. *Neuron* **87**, 492–506 (2015).

14. Mitchison, T. & Kirschner, M. Dynamic instability of microtubule growth. *Nature* **312**, 237–242 (1984).

15. Desai, A. & Mitchison, T. J. Microtubule polymerization dynamics. *Annu. Rev. Cell Dev. Biol.* **13**, 83–117 (1997).

16. Gavriljuk, K. *et al.* A synthetic morphogenic membrane system that responds with self-organized shape changes to local light cues. *bioRxiv* 481887 (2019) doi:10.1101/481887.

17. Howard, J. & Hyman, A. A. Dynamics and mechanics of the microtubule plus end. *Nature* vol. 422 753–758 (2003).

18. Bodakuntla, S., Jijumon, A. S., Villablanca, C., Gonzalez-Billault, C. & Janke, C. Microtubule-Associated Proteins: Structuring the Cytoskeleton. *Trends in Cell Biology* vol. 29 804–819 (2019).

19. Daub, H., Gevaert, K., Vandekerckhove, J., Sobel, A. & Hall, A. Rac/Cdc42 and p65PAK regulate the microtubule-destabilizing protein stathmin through phosphorylation at serine 16. *J. Biol. Chem.* **276**, 1677–1680 (2001).

20. Leung, T., Manser, E., Tan, L. & Lim, L. A novel serine/threonine kinase binding the Ras-related RhoA GTPase which translocates the kinase to peripheral membranes. *J. Biol. Chem.* **270**, 29051–29054 (1995).

21. Manser, E., Leung, T., Salihuddin, H., Zhao, Z. S. & Lim, L. A brain serine/threonine protein kinase activated by Cdc42 and Rac1. *Nature* **367**, 40–46 (1994).

22. Curmi, P. A. *et al.* The stathmin/tubulin interaction in vitro. *J. Biol. Chem.* **272**, 25029–25036 (1997).

23. Axelrod, D. & Wang, M. D. Reduction-of-dimensionality kinetics at reaction-limited cell surface receptors. *Biophys. J.* **66**, 588–600 (1994).

24. Adam, G. & Delbrück, M. Reduction of dimensionality in biological diffusion processes. in *Structural chemistry and molecular biology* 198–215 (W. H. Freeman and Co., 1968).

25. Rangamani, P. *et al.* Decoding information in cell shape. *Cell* **154**, 1356–1369 (2013).

26. Schmick, M. & Bastiaens, P. I. H. The interdependence of membrane shape and cellular signal processing. *Cell* **156**, 1132–1138 (2014).

27. Lämmermann, T. *et al.* Neutrophil swarms require LTB4 and integrins at sites of cell death in vivo. *Nature* **498**, 371–375 (2013).

28. Ng, L. G. *et al.* Visualizing the neutrophil response to sterile tissue injury in mouse dermis reveals a three-phase cascade of events. *J. Invest. Dermatol.* **131**, 2058–2068 (2011).

29. Afonso, P. V. *et al.* LTB4 Is a Signal-Relay Molecule during Neutrophil Chemotaxis. *Dev. Cell* **22**, 1079–1091 (2012).

30. Yu, H., Lim, K. P., Xiong, S., Tan, L. P. & Shim, W. Functional Morphometric Analysis in Cellular Behaviors: Shape and Size Matter. *Adv. Healthc. Mater.* **2**, 1188–1197 (2013).

31. Lobo, J., See, E. Y.-S., Biggs, M. & Pandit, A. An insight into morphometric descriptors of cell shape that pertain to regenerative medicine. *J. Tissue Eng. Regen. Med.* **10**, 539–553 (2016).

32. Albertini, M. C. *et al.* Automated analysis of morphometric parameters for accurate definition of erythrocyte cell shape. *Cytometry* **52A**, 12–18 (2003).

33. Keren, K. *et al.* Mechanism of shape determination in motile cells. *Nature* **453**, 475–480 (2008).

34. Ma, X., Dagliyan, O., Hahn, K. M. & Danuser, G. Profiling cellular morphodynamics by spatiotemporal spectrum decomposition. *PLoS Comput. Biol.* **14**, e1006321 (2018).

35. Driscoll, M. K. *et al.* Cell Shape Dynamics: From Waves to Migration. *PLoS Comput. Biol.* **8**, e1002392 (2012).

36. Zicha, D. *et al.* Rapid actin transport during cell protrusion. *Science (80-.).* **300**, 142–145 (2003).

37. Biyasheva, A., Svitkina, T., Kunda, P., Baum, B. & Borisy, G. Cascade pathway of filopodia formation downstream of SCAR. *J. Cell Sci.* **117**, 837–848 (2004).

38. Ji, L., Lim, J. & Danuser, G. Fluctuations of intracellular forces during cell protrusion. *Nat. Cell Biol.* **10**, 1393–1400 (2008).

39. Machacek, M. *et al.* Coordination of Rho GTPase activities during cell protrusion.

Nature **461**, 99–103 (2009).

40. Yang, H. W., Collins, S. R. & Meyer, T. Locally excitable Cdc42 signals steer cells during chemotaxis. *Nat. Cell Biol.* **18**, 191–201 (2016).
41. Benedetti, L. *et al.* Light-activated protein interaction with high spatial subcellular confinement. *Proc. Natl. Acad. Sci. U. S. A.* **115**, E2238–E2245 (2018).
42. Pathak, G. P., Strickland, D., Vrana, J. D. & Tucker, C. L. Benchmarking of optical dimerizer systems. *ACS Synth. Biol.* **3**, 832–838 (2014).
43. Guntas, G. *et al.* Engineering an improved light-induced dimer (iLID) for controlling the localization and activity of signaling proteins. *Proc. Natl. Acad. Sci. U. S. A.* **112**, 112–117 (2015).
44. Wu, Y. I. *et al.* A genetically encoded photoactivatable Rac controls the motility of living cells. *Nature* **461**, 104–108 (2009).
45. Milias-Argeitis, A. *et al.* In silico feedback for in vivo regulation of a gene expression circuit. *Nat. Biotechnol.* **29**, 1114–1116 (2011).
46. Milias-Argeitis, A., Rullan, M., Aoki, S. K., Buchmann, P. & Khammash, M. Automated optogenetic feedback control for precise and robust regulation of gene expression and cell growth. *Nat. Commun.* **7**, 12546 (2016).
47. Toettcher, J. E., Gong, D., Lim, W. A. & Weiner, O. D. Light-based feedback for controlling intracellular signaling dynamics. *Nat. Methods* **8**, 837–839 (2011).
48. Harrigan, P., Madhani, H. D. & El-Samad, H. Real-Time Genetic Compensation Defines the Dynamic Demands of Feedback Control. *Cell* **175**, 877-886.e10 (2018).
49. Perkins, M. L., Benzinger, D., Arcak, M. & Khammash, M. Cell-in-the-loop pattern formation with optogenetically emulated cell-to-cell signaling. *Nat. Commun.* **11**, 1–10 (2020).
50. Niederholtmeyer, H., Chaggan, C. & Devaraj, N. K. Communication and quorum sensing in non-living mimics of eukaryotic cells. *Nat. Commun.* **9**, (2018).
51. Toda, S., Blauch, L. R., Tang, S. K. Y., Morsut, L. & Lim, W. A. Programming self-organizing multicellular structures with synthetic cell-cell signaling. *Science (80-.).* **361**, 156–162 (2018).
52. Gradinaru, C. Stochastic models of cell motility. *Tech. Univ. Denmark* (2012).

53. Abkarian, M., Loiseau, E. & Massiera, G. Continuous droplet interface crossing encapsulation (cDICE) for high throughput monodisperse vesicle design. *Soft Matter* **7**, 4610 (2011).

54. Pinot, M. *et al.* Effects of confinement on the self-organization of microtubules and motors. *Curr. Biol. CB* **19**, 954–960 (2009).

55. Gradinaru, C. *et al.* Assessment of automated analyses of cell migration on flat and nanostructured surfaces. *Computational and Structural Biotechnology Journal* vol. 1 e201207004 (2012).

56. Campos, D., Méndez, V. & Llopis, I. Persistent random motion: Uncovering cell migration dynamics. *J. Theor. Biol.* **267**, 526–534 (2010).

57. Gail, M. H. & Boone, C. W. The Locomotion of Mouse Fibroblasts in Tissue Culture. *Biophys. J.* **10**, 980–993 (1970).

58. Grassé, P.-P. La Reconstruction du nid et les coordinations interindividuelles chez Bellicositermes natalensis et Cubitermes Sp. ; la théorie de la stigmergie : essai d'interprétation, comportement des termites constructeurs. *Insectes Soc.* **6**, 41–81 (1959).

59. Guevorkian, K., Manzi, J., Pontani, L.-L., Brochard-Wyart, F. & Sykes, C. Mechanics of Biomimetic Liposomes Encapsulating an Actin Shell. *Biophys. J.* **109**, 2471–2479 (2015).

60. Steinberg-Yfrach, G. *et al.* Light-driven production of ATP catalysed by F0F1-ATP synthase in an artificial photosynthetic membrane. *Nature* **392**, 479–482 (1998).

61. Berhanu, S., Ueda, T. & Kuruma, Y. Artificial photosynthetic cell producing energy for protein synthesis. *Nat. Commun.* **10**, (2019).

62. Borowiak, M. *et al.* Optical Manipulation of F-Actin with Photoswitchable Small Molecules. *J. Am. Chem. Soc.* **142**, 9240–9249 (2020).

63. Prevedel, R. *et al.* Simultaneous whole-animal 3D imaging of neuronal activity using light-field microscopy. *Nat. Methods* **11**, 727–730 (2014).

64. Prevedel, R. *et al.* Fast volumetric calcium imaging across multiple cortical layers using sculpted light. *Nat. Methods* **13**, 1021–1028 (2016).

65. Wagner, N. *et al.* Instantaneous isotropic volumetric imaging of fast biological

processes. *Nat. Methods* **16**, 497–500 (2019).

ACKNOWLEDGEMENTS

I would like to thank my supervisor Philippe, for his trust and support, for encouraging me to generate creative ideas, and for pushing us to “jump over our own shadow”.

I would like to thank all the people at the Department of Systemic Cell Biology for their openness, great company and discussions. Many thanks to Lisaweta, Jutta, Manu and Hendrike for lots of help in the transition to molecular biology. I also want to thank Marton, Wayne, Antonios, Klaus, Sven, Malte, Amit, Dhruv and Yannick for great times and all their support.

I would like to thank all the people of the MaxSynBio Project, Konstantin, Farid, Hans, Malte, Aneta, Akhilesh and of course, Philippe. It was fantastic to work with all of you together as a team. I learned a lot from all of you, humanly and scientifically. I am very thankful of having been able to contribute to such an amazing project, which gave me the opportunity of understanding how a truly interdisciplinary project is put forward; how synergy between disciplines comes about. I enjoyed very much having undertaken this challenge with all you together.

Special thanks to Konstantin Gavriljiuk, for being himself, Hans Seidel, for his lovely company, Farid Ghasemalizadeh, for his unmatched happy charm, Angel Stanoev, for wonderful scientific and non-scientific discussions, Jan Hübinger, for his timeless wisdom, and Michael Reichl, por su sensibilidad humana.

I would also like to thank Düsseldorf, for being an inspiring city.

Ich möchte mich bei der Familie Hennes bedanken, meine Familie in Deutschland.

A mis amigos, Rodri, Fede, Nacho, Javi y Martin.

A la abuela y anti, mama y papa, y al bro.

And to my love Elisabeth.